Chaotic dynamics in open flow: The excited jet

Marco Bonetti
von Karman Institute, 72 Chée de Waterloo, 1640 Rhode St. Genese, Belgium
*and Université Libre de Bruxelles, Code Postal 231, Boulevard du Triomphe, 1050 Bruxelles, Belgium**

Jean-Pierre Boon
*Université Libre de Bruxelles, Code Postal 231, Boulevard du Triomphe, 1050 Bruxelles, Belgium**
(Received 10 April 1989)

We present a dynamical system analysis of an experimental study on an axisymmetrical excited air jet. The transition to turbulence—*weak turbulence*—is investigated by imposing on the laminar flow a controlled excitation which triggers the spatial development of the jet instability. By longitudinal and azimuthal coherence and phase measurements, we find that a helical structure with azimuthal mode $m = \pm 1$ is being selected, in accordance with spatial linear stability analysis. Further downstream, the transition to turbulence is evidenced, through a decrease in spatial coherence, by destabilization and a breakdown of the helical structure. We analyze the transition to turbulence with the techniques of dynamical systems theory. The presence of an initial helical structure in the flow suggests that the chaotic dynamics has low dimensionality: the *correlation dimension* computed along the jet axis ($18\phi \leq l \leq 24\phi$, where ϕ is the nozzle diameter) at $R = 543$ shows that the dimension of the chaotic attractor increases continuously from ~ 3 to ~ 6. Good correlation is found between spatial coherence and attractor dimension, which confirms the validity of the values obtained for the chaotic attractor dimensionality. From *local coherence* measurements, we infer a power-law dependence between the attractor dimension and the *local correlation length* (the range of the local turbulent structure). This result clearly indicates that in *open* systems the attractor dimension (as computed from time series data) is to be connected to the local chaotic dynamics of the flow.

I. INTRODUCTION

Chaotic temporal behavior in *closed systems* governed by an *absolute instability* (zero group velocity of a disturbance) is nowadays well documented. Systems such as Rayleigh-Bénard (RB) convection or Couette-Taylor flow between rotating cylinders have been studied extensively and are presently quite well understood. For RB convection in small geometry, chaotic flow corresponds to motion on a chaotic attractor of low dimensionality.[1] This low finite value is a consequence of the high confinement imposed by the boundaries on the internal flow which results in a strong coupling between modes. This gives rise to a spatially highly coherent "frozen" flow, which can therefore be described by a single chaotic attractor.

In large aspect ratio RB systems (large in the two horizontal directions), the chaotic state is generated by the competition between different unstable modes; the dynamics can be described by several localized chaotic attractors in the flow.[2] The secondary instabilities which develop on the primary instability tridimensionalize the flow by introducing a vertical vorticity component.[3] Turbulence in such confined systems is thus essentially *spatio-temporal* with a loss of spatial coherence in the flow. It is only recently that the spatial coherence function between adjacent points in the flow—a measure of the degree of linear correlation between fluctuations—has been related to the local attractor dimension while a control parameter is varied.[4]

The transition to *fully developed* turbulence is generally investigated in *open systems* whose initial instability is generated by large velocity gradients normal to the mean flow [e.g., quasi-two-dimensional (2D) mixing layer, 2D and 3D jets and wakes]. Such systems are generally dominated by a *convective instability* (the group velocity of the perturbation is nonzero and the edges of the perturbation travel in the same direction) and a spatial stability analysis must therefore be used.

In open systems we observe typically a region of spatial exponential growth of the most unstable mode (domain of linear stability), followed by a nonlinear saturation of the mode which generates advected *coherent structures* (CS) and finally a 3D destabilization and a breakdown into eddies of these macroscopic CS (Ref. 5). If we suppose that the flow is initially quasi-2D, the last sequence of the destabilization process leads—far downstream—to a homogeneous and isotropic turbulence with a velocity power spectrum continuous in frequency and wave number.

The understanding of the destabilization and breakdown process of the coherent structures is of fundamental importance for a correct analysis of the fully turbulent flow field which follows the transitional regime. In fact, with modern techniques of data reduction such as conditional sampling,[6] it is recognized experimentally that re-

sidual CS are still persistent in the self-similar fully turbulent zone where it is generally accepted that the flow is independent of initial conditions.

As a first approach to the transition from laminar to turbulent regime, one can consider that, near the marginal stability, the flow is *weakly* nonlinear. The Ginzburg-Landau equation can be used to model the spatio-temporal nonlinear evolution of hydrodynamic marginal waves.[7] Although widely used in confined systems,[8] this approach has been applied only recently to open systems. Provansal *et al.* have shown that in a 2D wake, the transverse velocity fluctuation near marginality follows a Landau-type description.[9]

The work presented here was undertaken in order to study the *highly nonlinear* transitional regime in an open flow: the excited air jet. By generating artificially a highly coherent structure in an open flow—free from any random perturbation—we can explore under well-controlled experimental conditions the spatial destabilization of such structure. The turbulent transition so observed—herein called *weak turbulence*—should be similar to the transition in free open flows, but occurs at a value of the Reynolds number R several orders of magnitude smaller than in the free case. The analysis is carried out for a value of the control parameter far above the critical value, $(R-R_c)/R_c \simeq 13.3$, and is based on dynamical systems theory. One particular purpose of the research is to investigate the relation between *spatial order*—corresponding to a high spatial correlation in the flow—and the dimension of the chaotic attractor.

In Sec. II we describe the experimental setup and present some flow visualizations. We discuss in Sec. III the spatial development of the flow structure and in Sec. IV, we investigate the destabilization of the flow structure in the weakly turbulent regime in connection with the existence of a chaotic attractor. In Sec. V we show that the chaotic attractor can describe the *statistics* of the local spatio-temporal dynamics over a length scale comparable to the *local* spatial correlation length scale. Section VI is devoted to a discussion—via the *bicoherence function*—of the longitudinal evolution of the quadratic coupling between modes.

II. EXPERIMENTAL ASPECTS AND FLOW VISUALIZATION

Transition to turbulence in open flows always involves a spatial destabilization of coherent structures triggered initially by a random perturbation which falls inside the marginal stability curve.[10] In order to realize a fast transitioning flow and to perform reproducible tests, an isothermal, air into air, axisymmetric laminar jet is externally excited. We define a *laminar* jet as an axisymmetric shear flow whose velocity profile varies as $U(r^*) = U_{CL}/(1+r^{*2})^2$ where U_{CL} is the center-line velocity and $r^* = r/r_0$ is the nondimensional radial distance [r_0 is the measure of the jet radial spread, defined by $U(r_0) = U_{CL}/4$]. Experimentally, such a free flow can be obtained in the self-similar zone of a jet with an initial Poiseuille velocity profile.[11]

We used an axisymmetric pipe of length $L/D = 71$, where $D = 6.25$ mm is the internal diameter of the pipe. This length is sufficient to ensure a well-established Poiseuille velocity profile at the pipe outlet.[12] A convergent entrance with a contraction ratio $\Gamma = 164$ uniformizes the flow at the pipe inlet and reduces the residual internal turbulence. Mass flow is maintained at a constant rate by a self-regulated microvalve which reduces Reynolds number fluctuations to less than 0.1%. Technically, the maximum Reynolds number, defined as $R = UD/\nu_s$ (where U is the mean axial velocity and ν_s is the kinematic viscosity) is ~ 700 which corresponds to an exit velocity of 3.4 m/s at the center line of the pipe.

The external excitation is realized by longitudinally vibrating the pipe together with the convergent duct and the longitudinal displacement is monitored by means of a displacement transducer. When applying a sinusoidal vibration, the rms of the center-line velocity fluctuation at the pipe outlet was shown to be linear with the displacement amplitude.

In order to eliminate any mechanical random vibration, the setup is positioned on an antivibrating table, and so as to avoid extraneous pressure fluctuations, the whole system is enclosed into an anechoic chamber with an internal noise level less than 50 dB.

Since the flow has no initial swirl, axial velocity measurements are performed with a simple hot wire: length $l/d = 200$, where $d = 5$ μm is the wire diameter. Before each set of measurements the hot wire is calibrated *in situ* within the expected velocity range. The frequency response was checked with a square wave test to be $\simeq 40$ kHz which is sufficient compared to the maximum frequency in the velocity fluctuation (from velocity power spectra, the frequency where the power is between -60 and -70 dB, is $\simeq 500$ Hz, see also Sec. IV). The signal was postlinearized after data acquisition through a 12 bit analog digital converter (ADC) on a VAX 11/780 computer. Further information concerning acquisition parameters will be given when useful. The hot-wire technique was chosen in preference to the nonintrusive laser Doppler velocimetry (LDV) technique mainly for two reasons: one is to avoid the flow seeding problem in LDV, and the other is that there is a constant acquisition frequency set by the ADC. In LDV, the arrival time of the seeding particles in the intersection volume of the two laser beams is supposed to be Poisson distributed; so we have a Poisson-distributed pseudoacquisition frequency at the photomultiplier. Here random sampling will cause a technical problem. Indeed, we want to reconstruct the attractor in phase space and compute its dimension from a single time series using the time delay technique; we also use fast Fourier transform (FFT) analysis:[13] all these techniques require a constant sampling time.

We have compared our mean velocity measurements (null excitation) with those of Rankin *et al.*[14] obtained by LDV in a water into water laminar jet with $L/D = 383$. In Figs. 1(a) and 1(b) we show the normalized velocity profile and the longitudinal evolution of the center-line velocity. As the comparison shows excellent agreement, we are confident that the hot-wire probe does not significantly perturb the flow field. From these measure-

ments, the nonexcited laminar jet is recognized to be *self-similar* for the mean velocity from an axial distance $X_c=(X/D)/R_s\simeq 0.018$ where $R_s=U_{CL}D/\nu_s$ with U_{CL} the center-line velocity at the pipe exit.[14]

Flow-visualizations were performed by longitudinal laser light sheet cuts of the seeded jet (condensed oil vapor), with and without excitation. Figure 2(a) shows that the free jet at $R=500$ remains stable up to downstream distances $X/D\leq 70$, whereas stability analysis by Morris[15] predicts that the most unstable mode—the *simple helical mode*—has a critical Reynolds number as low as $R_c\simeq 38$. That the jet be stable here at $R=500$ confirms that the flow is indeed free from random perturbations and that the inlet flow has a very weak residual turbulence (at $X/D=36$ and $R=370$ without excitation, no velocity fluctuations could be observed on the oscilloscope).

Figures 2(b) and 2(c) show stroboscopic (at the excitation frequency) flow visualizations for two amplitudes of excitation. Spatially evolving structures are observed. One distinguishes a three-regime sequence: (i) a *laminar* region dominated by stationary macroscopic structures, (ii) a *weakly turbulent* zone where the structures are no longer steady in time (despite the stroboscopic visualiza-

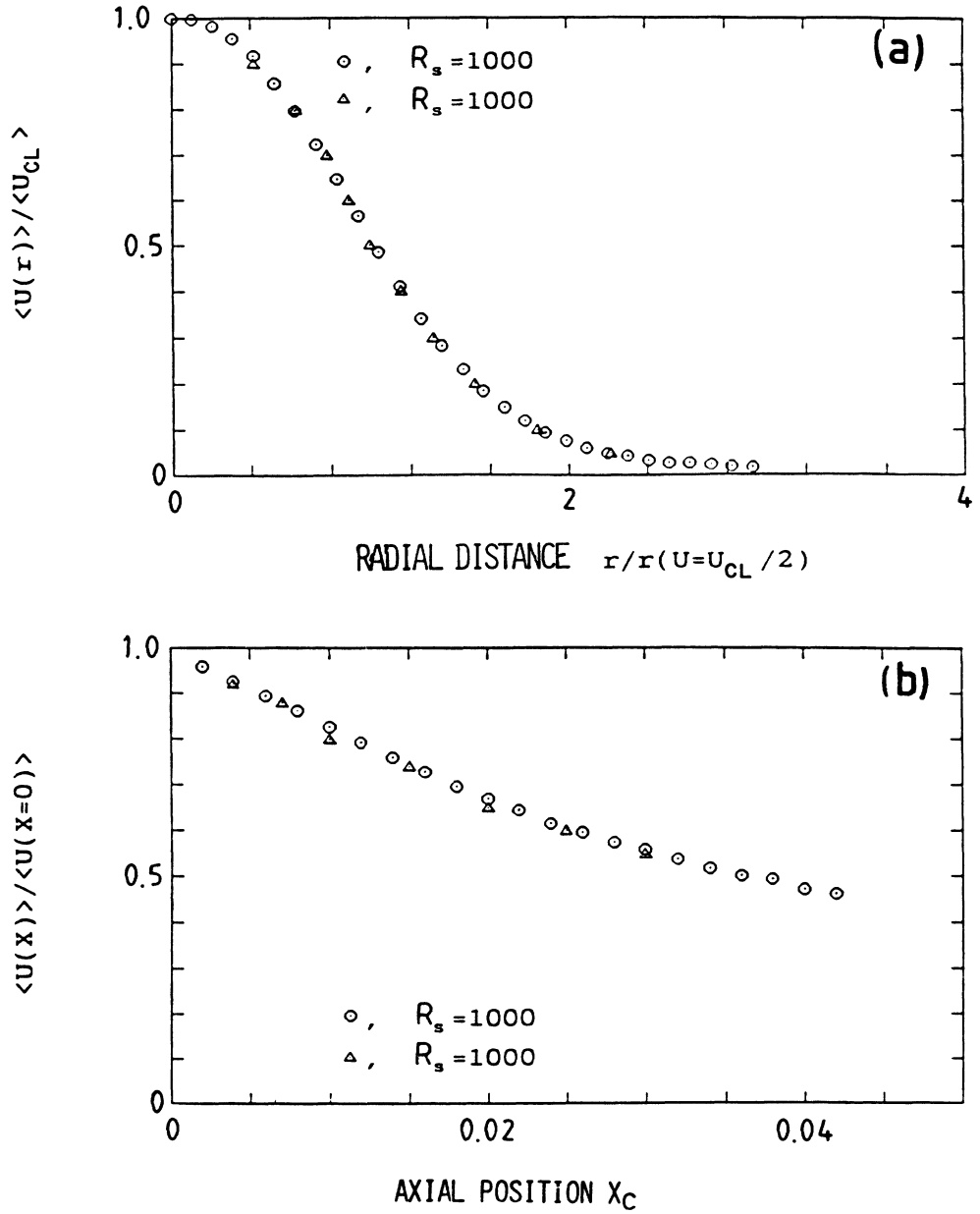

FIG. 1. (a) Radial profile of the mean axial velocity, normalized by the center-line mean axial velocity. Longitudinal probe position, $X_c=0.005$. (b) Longitudinal evolution of the mean axial velocity, normalized by the mean velocity at $X_c=0$. Open circles: present measurements (null excitation) with $R_s=1000$; open triangles: measurements from Rankin *et al.* (Ref. 14), $R_s=1000$.

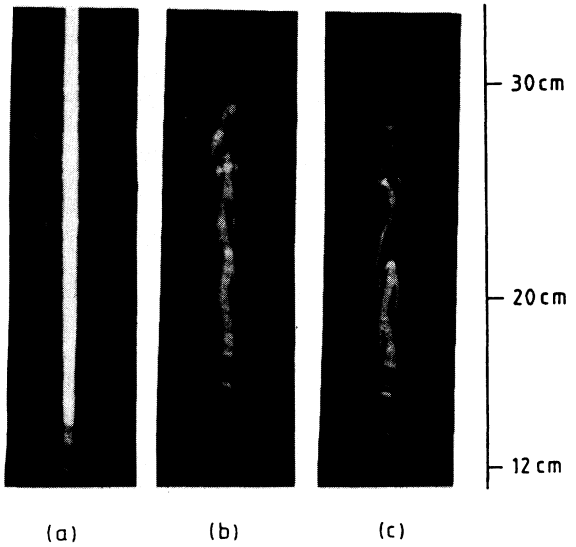

FIG. 2. Laser-light sheet flow visualization of the seeded jet. (a) The nonexcited jet at $R=500$. Top of scale is located at $X/D=61$. (b) and (c) Stroboscopic flow visualization of the excited seeded jet: $f_0=20$ Hz, $R=500$, normalized rms velocity fluctuation $u/U=0.4\%$ (b) and 0.6% (c). Notice the weakly turbulent region where the helical structure is no longer visible.

tion), and (iii) a *turbulent* zone where the structures have disappeared and an important mixing process takes place. Increasing the excitation amplitude shortens the laminar and transition regions and enhances the turbulent one, but does not modify qualitatively the sequence. Furthermore, the same spatial pattern holds for a range of excitation frequencies (20–40 Hz). These flow visualizations, by showing the different flow regimes, clearly indicate the convective nature of the instability.

III. FLOW STRUCTURE AND NORMAL MODE ANALYSIS

A. Linear stability analysis: Comparison of experiments with prediction

The flow being axisymmetric (along the x direction) any perturbation can be written as

$$A(r^*)\exp i(\alpha x-\omega t+m\theta)$$

where $A(r^*)$ is the r^*-dependent amplitude, α is the complex wave number, ω (real) represents the frequency of the perturbation, and m is the azimuthal mode number, θ being the azimuthal angle. $m=0$ corresponds to the axisymmetric mode (i.e., the vortex ring), $m=\pm1$ to the simple left and right helical modes, $m=\pm2$ to the double left and right helical modes,. . . . In a laminar jet, modes $m=0$ and ±2 have been recognized to be more stable than the mode $m=\pm1$.[16]

Morris[15] has performed a linear spatial viscous stability analysis of an axisymmetric laminar jet by computing the spatial growth rate $-\alpha_i$ for the simple helical mode. The main results of the analysis are the following: (i) there exists a curve of *marginal stability* ($\alpha_i=0$) in the (ω,R) plane which gives a critical Reynolds number $R_c\simeq38$ below which the simple helical mode is stable whatever the frequency of the perturbation and (ii) the flow is dominated by a *viscous instability* since, for a finite range of R, the simple helical mode has a maximum spatial amplification rate [existence of a closed curve of constant spatial amplification in the plane (ω,R)]. We shall now check these spatial linear stability predictions against our experimental results.

It is generally accepted that the linear approach is valid as long as $u/U\leq2\%$ (Ref. 17) where u is the rms velocity fluctuation. In our experiments, the excitation amplitude was kept sufficiently low in order to satisfy the above "linear" conditions. The jet was excited at several frequencies ranging from 15 to 70 Hz. For each excitation frequency, the Reynolds number was increased slowly step by step, with $\Delta R=25$, and at each Reynolds number increment the velocity fluctuations were recorded. The hot-wire probe was positioned in the self-similar zone such that $X_c\geq0.018$ and, according to the excitation frequency, so as to get significant velocity fluctuations. Using a multibandpass digital filter with frequency window $\Delta f=1$ Hz, we measured the rms of the velocity components at the excitation frequency f_0 and its harmonics. In Fig. 3, we show the normalized rms velocity fluctuations as a function of R, respectively for an excitation frequency $f_0=20$ and 30 Hz. Since the measuring position is fixed in space, one can speak equivalently of the rms value of the fluctuations or of the spatial amplification rate α_i. One observes that this quantity reaches an absolute maximum for a finite value R, which evidences the viscous character of the instability (the spatial amplification rate is larger at a finite value of the Reynolds number than at $R=\infty$).

We compared our experimental results with Morris's predictions.[15] From normalized radial velocity profiles measured in the self-similar zone ($X_c\simeq0.018$) and without excitation, the characteristic radius r_0 is estimated to be $r_0\simeq4.5$ mm for $250\leq R\leq500$. In Fig. 4 we plot the frequency of the disturbance as a function of the value of R at which the largest spatial growth rate is obtained. Figure 4 shows our experimental results (labeled by letters) along with data from Morris's analysis for the simple helical mode with either $r_0=2.8$ or 4.5 mm. Experimental points A, B, C, and D measured at $X_c=0.018$ are in agreement with the linear prediction if $r_0=2.8$ mm is used. This discrepancy with the estimated value (4.5 mm) could be due to contamination of the simple azimuthal mode $m=\pm1$ by the axisymmetric mode $m=0$ still present in the flow. In fact, at point E ($X/D=16$) the amplitude ratio between the helical and axisymmetric modes is $A_1/A_0\simeq3$ (see Sec. III B). The persistence at this position of the axisymmetric mode does not allow therefore a direct comparison with Morris's analysis performed for the mode $m=\pm1$ alone. Data labeled F–K show the influence of the shape of the velocity profile on the jet instability (these data were obtained in the development region $X_c\leq0.018$). In particular, points G, H, and I were measured at $X_c=0.003$, 0.010, and 0.016, re-

spectively, based on $R_s = 2R^*$, where R^* corresponds to the largest spatial amplification rate. One observes that as the measuring position moves downstream, R^* increases in value towards the linear prediction: again, this could be a consequence of the influence of the flow structure on the overall stability characteristics. We performed measurements further downstream in order to capture the instability of the simple helical mode alone; however, for such positions the velocity fluctuations exceed 2% and consequently the linear stability analysis breaks down.

B. Spatial development of the flow structure

We now investigate the longitudinal evolution of the mean wavelength of the disturbance and show how the flow structure observed in the laminar zone can be decomposed into normal modes. We used the cross-spectrum technique which consists in computing the Fourier transform of the cross-correlation function $\mathcal{R}_{ij}(\tau) = E[x_i(t)x_j(t+\tau)]$ between two random, stationary, and real variables $x_i(t)$ and $x_j(t)$ (E denotes the expectation). The complex Fourier transform reads[18]

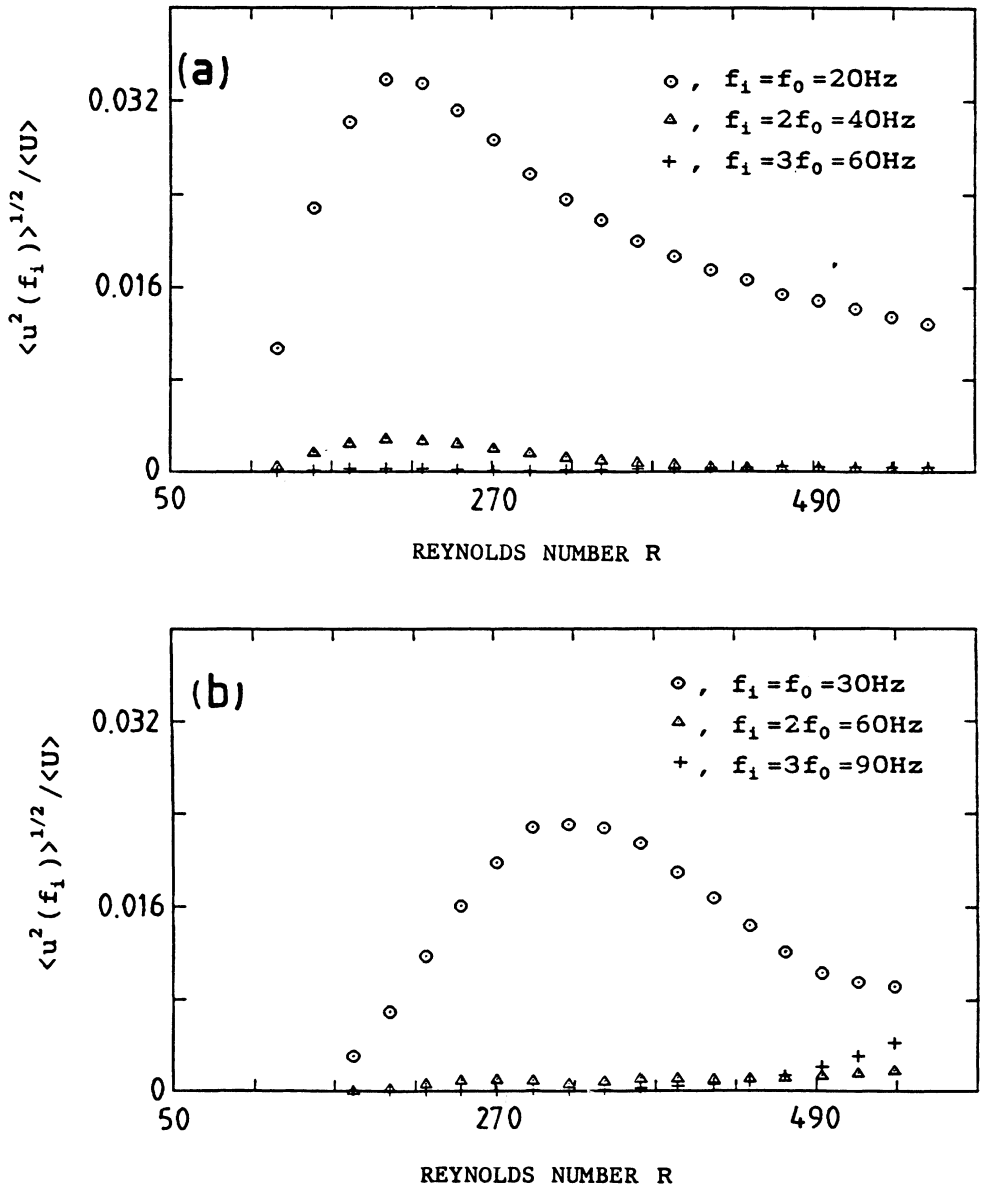

FIG. 3. Rms axial velocity fluctuation components, normalized by the local mean velocity, as a function of R, for excitation frequency f_0 and harmonics $2f_0$ and $3f_0$. (a) $f_0 = 20$ Hz, normalized rms velocity $u/U = 1.6\%$, $R = 150$; longitudinal probe position $X/D = 7.8$, center-line radial position. (b) $f_0 = 30$ Hz, $u/U = 1.5\%$, $R = 200$; $X/D = 11.7$ and center-line radial position.

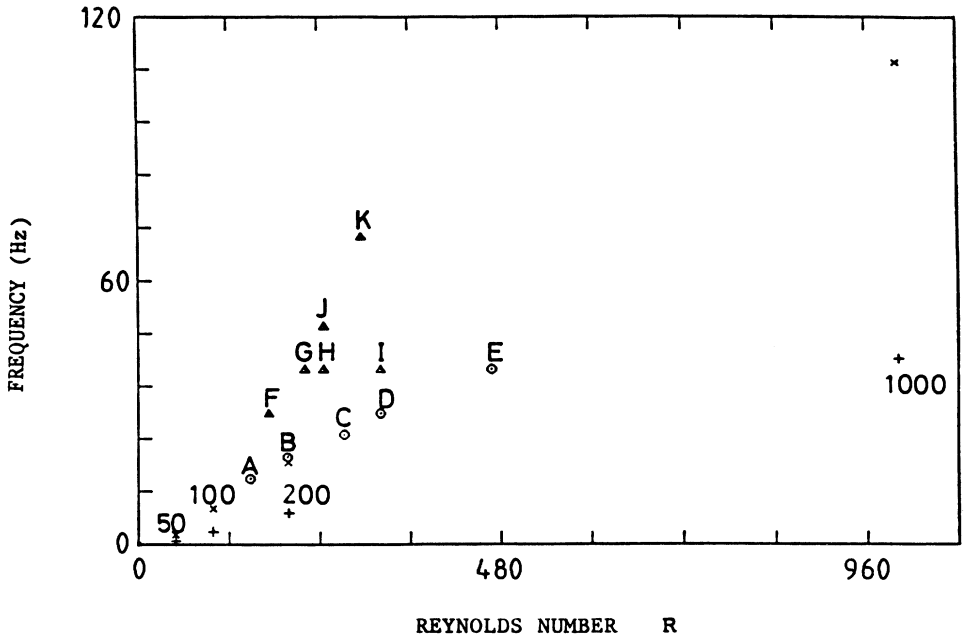

FIG. 4. Frequency of the applied disturbance as a function of R for which the disturbance experiences the largest spatial amplification. Crosses: Morris's computation (Ref. 15) at $R=50$, 100, 200, and 1000, with a characteristic radius $r_0(U=U_{CL}/4)=2.8$ mm ($\times$); and $r_0=4.5$ mm ($+$). Present experimental points: open circles labeled A, B, C, D, and E were measured in the self-similar region with a normalized axial position $X_c\simeq 0.018$; open triangles labeled F, G, H, I, J, and K were measured in the development region of the jet with normalized axial position $X_c=0.004$ (F), 0.003 (G), 0.010 (H), 0.016 (I), 0.003 (J), and 0.003 (K).

$$P_{ij}(f)=F(\mathcal{R}_{ij}(\tau))$$
$$=C_{ij}(f)+iQ_{ij}(f)$$
$$=|P_{ij}(f)|e^{i\varphi(f)}$$

where $\varphi(f)=\arctan[Q_{ij}(f)/C_{ij}(f)]$ is the phase shift between the variables x_i and x_j at frequency f. The normalized coherence function is defined by

$$\gamma(f)=\frac{C_{ij}^2+Q_{ij}^2}{P_{ii}P_{jj}}$$

where P_{ii} and P_{jj} are the power spectra of the random variables x_i and y_j, respectively. When $\gamma(f)=1$, the x_i and x_j variables are linearly correlated while, when $\gamma(f)=0$, the two variables are totally uncorrelated at frequency f.

In the present experiment, the coherence function is used to localize the laminar region in the jet, and the phase shift to compute the longitudinal wavelength of the disturbance (by *longitudinal* cross correlations) and to decompose the flow structure into azimuthal modes (by *azimuthal* cross correlations). We cross correlated the velocity fluctuations with the displacement of the vibrating apparatus which is used as the reference signal. Special care must be taken when estimating the cross-power spectra. In order to reduce the variance of the phase shift and of the coherence estimators,[19] power spectra are averaged and 24 fast-Fourier transforms (FFT's) are computed over 1024 data points each, which gives a frequency resolution $\Delta f=3.05$ Hz.

Longitudinal cross correlations. Figure 5 shows the longitudinal evolution of the coherent function $\gamma(f)$ and of the phase shift $\varphi(f)$ for an excitation at $f_0=40$ Hz and $R=426$. From the coherence plot, two distinct regions are observable: the region where $\gamma(f)=1$ indicates a perfect correlation between the velocity fluctuations and the excitation. This region is to be related to the laminar zone of the jet while the transitional zone is characterized by the region of coherence decay. A low value of the coherence function indicates a destabilization of the coherent structure which is therefore less linearly correlated to the excitation.

The phase shift $\varphi(f)$ (defined mod 2π) varies linearly with the axial position X/D in the region where the coherence function is high valued. This behavior is a clear indication of a spatial periodicity in the flow; the corresponding change in slope shows a downstream longitudinal decrease of the wavelength [see Fig. 5(b)]. Figure 6 shows the axial evolution of the Strouhal number $S=f_0\lambda/U_{CL}$ evaluated with the mean wavelength λ of the disturbance and the center-line mean velocity U_{CL} at the pipe exit, for several excitation frequencies and Reynolds numbers. The wavelength is obtained from the phase shift variations [Fig. 5(b)]; λ represents a value averaged over a distance comparable to λ itself. Notice that the variation of the Strouhal number as a function of axial position follows a "universal" law, independently of

the excitation frequency and of R. Consequently, the jet should exhibit the same instability sequence under any excitation frequency; therefore in the remainder we shall report on experiments performed at one single excitation frequency, $f_0 = 40$ Hz.

Azimuthal cross correlation. The hot-wire probe is positioned in a circle (radius $r = 1$ mm) in a plane normal to the jet axis. The maximum azimuthal angle displacement is 180°, with an angle step $\Delta\theta = 10°$.

The longitudinal mechanical vibration induces at the pipe exit a velocity perturbation that is mainly axisymmetric ($m = 0$). We also assume that the jet can develop a left and right helical mode ($m = \pm 1$). However, here the generation mechanism of these modes is unknown; indeed, we do not trigger artificially the excitation of mode $m = \pm 1$ as did Cohen and Wygnanski.[20] In an idealized jet, the probabilities of occurrence of modes $m = +1$ and -1 should be equal, but in real experiments, small imperfections will enhance the development of one helical mode which will remain dominant far downstream. Assuming that the axisymmetric mode $m = 0$ and the helical modes $m = \pm 1$ are the only dominant

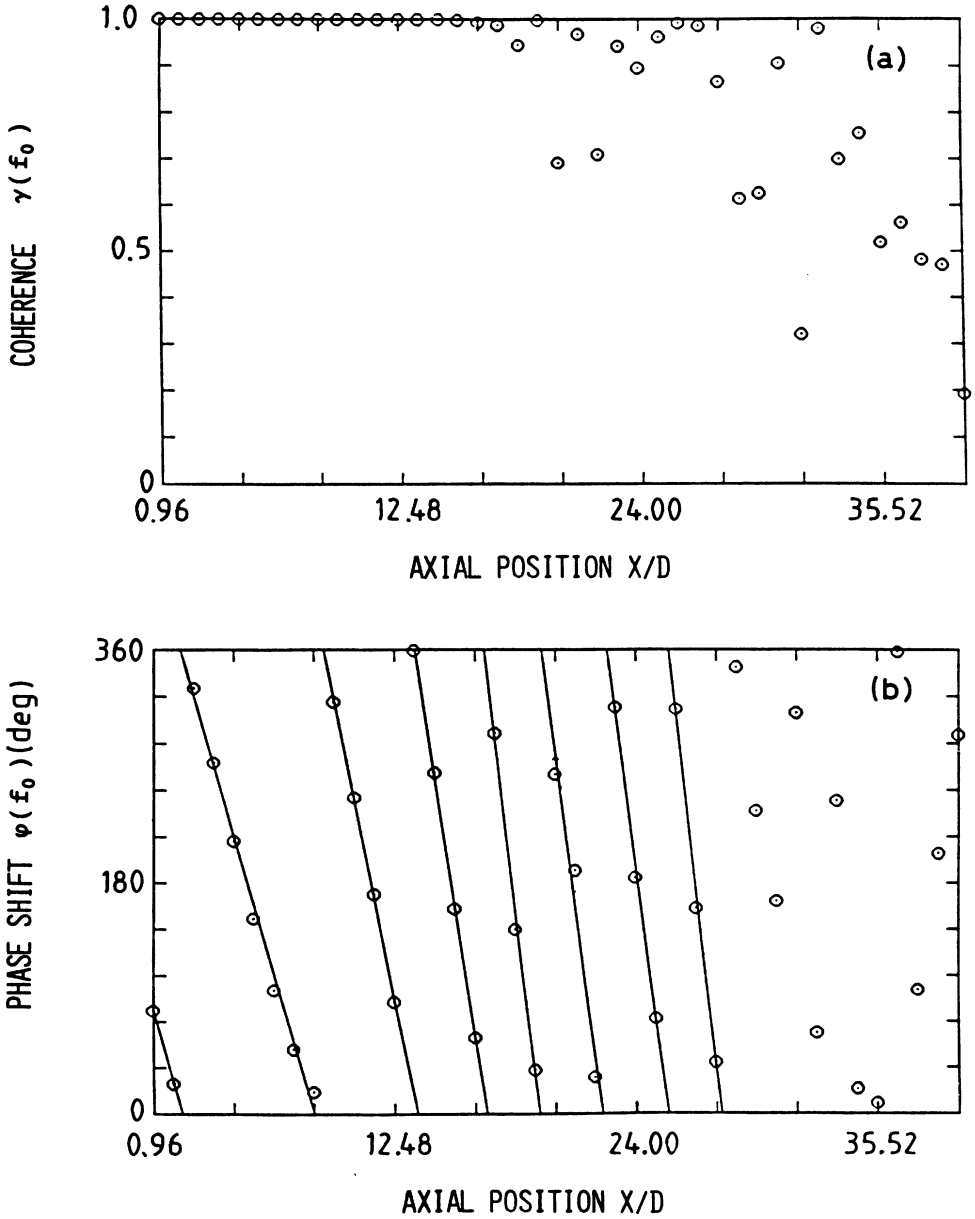

FIG. 5. The coherence (a) and the phase shift (b) between the velocity fluctuation component at frequency f_0 and the displacement signal, as a function of the axial position X/D. Excitation frequency: $f_0 = 40$ Hz; normalized rms velocity fluctuations: $u/U \simeq 1.2\%$; $Re = 426$, center-line radial position. Cross-power spectra were averaged over 24 FFT's.

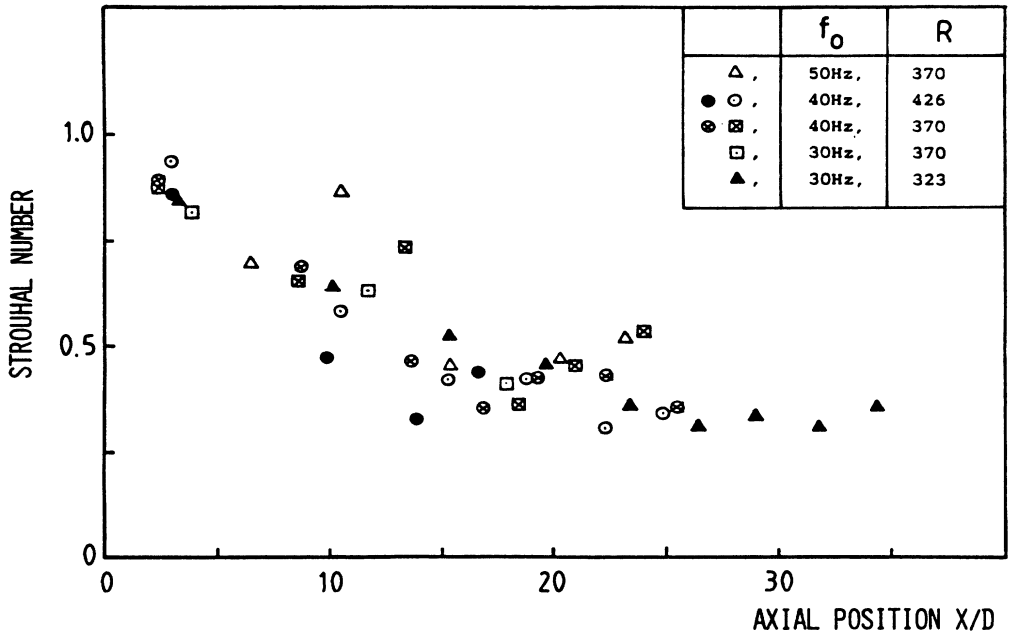

FIG. 6. Strouhal number (evaluated with the mean wavelength of the disturbance) as a function of the axial position X/D, for various excitation frequencies and Reynolds numbers.

modes, we can write the total velocity fluctuations in the linear regime as[21]

$$u(t)=A_0\exp i(-2\pi f_0 t+\alpha_0)+A_1\exp i(-2\pi f_0 t+\theta+\alpha_1)+A_{-1}\exp i(-2\pi f_0 t-\theta+\alpha_{-1}) .$$

Here $A_{\pm 1}$ represents the amplitude of the $m=\pm 1$ azimuthal mode and the α_i's denote the phases of the respective modes. By cross correlating $u(t)$ with the reference signal $s(t)=e^{i2\pi f_0 t}$ and taking the Fourier transform of the cross-correlation function, one obtains the cross spectrum

$$P_{us}(f)=A_0 e^{i\alpha_0}\delta(f-f_0)+A_1 e^{i(\alpha_1+\theta)}\delta(f-f_0)+A_{-1}e^{i(\alpha_{-1}-\theta)}\delta(f-f_0)$$

where $\delta(f-f_0)$ is the Dirac δ function.

It is clear why we have ignored the double helical mode $m=\pm 2$: this mode (with frequency $2f_0$) does not contribute to the fluctuations at f_0; the same applies to the higher-order azimuthal modes. From the relation given above, the phase shift at frequency f_0 reads

$$\varphi(f_0)=\frac{(A_1/A_0)\sin\theta-(A_{-1}/A_0)\sin\theta+\sin\alpha_0}{(A_1/A_0)\cos\theta+(A_{-1}/A_0)\cos\theta+\cos\alpha_0} .$$

Here we have set $\alpha_1=\alpha_{-1}=0$ i.e., the modes $m=\pm 1$ are assumed to be excited simultaneously. Given the azimuthal angle θ, the phase shift is a function of α_0 and of the amplitude ratios A_1/A_0 and A_{-1}/A_0. So by fitting the experimental phase shift with the theoretical $\varphi(f_0)$, we can determine the dominant modes from the mode amplitude ratios.

In Fig. 7 we show the theoretical and experimental phase shifts versus the azimuthal angle θ, for two axial positions ($X/D=16$ and 19.2) with $R=395$ and with excitation frequency $f_0=40$ Hz. The amplitudes of modes $m=\pm 1$ are set equal. From the fitting procedure, it appears that the flow structure is mainly composed of the first two azimuthal modes whose relative strength, in terms of the amplitude ratio, varies with the longitudinal position. At $X/D=16$, the best fit is obtained by setting $A_1/A_0\simeq 1.65$ while at $X/D=19$, the optimal amplitude ratio is $A_1/A_0\simeq 4.0$. These results confirm the linear stability analysis prediction that the flow selects the simple helical mode even though the injected disturbance at the pipe exit is initially axisymmetric.

The influence of the Reynolds number on the mode selection mechanism is seen from the comparison of Figs. 8 and 7. An increase of R ($R=494$, Fig. 8; 395, Fig. 7) enhances the growth of the helical mode: for the same axial position [Figs. 7(a) and 8(a)], the amplitude ratio A_1/A_0 goes from $\simeq 4.0$ for $R=395$ to $\simeq 10$ for $R=494$. Figure 8(b) shows that further downstream, the flow is *prevalently* dominated by only one mode, here $m=-1$ ($A_1/A_0\simeq 13.0$ and $A_{-1}/A_0\simeq 7.0$) and that the theoretical phase shift approaches a linear decay (with slope -1) as a function of the azimuthal angle.

Longitudinal evolution of the fluctuations. In order to follow, independently of the finite value of excitation amplitude, the longitudinal evolution of disturbance assumed to be initially infinitesimal, we Wiener-filtered the velocity fluctuations.[22] Here, the Wiener-filtering operation consists in subtracting from the velocity power spectrum the power contribution linearly related to the external excitation. Using the coherence function (see above), the power *not* linearly related to the excitation is given by

$$P_{uu}^{\mathrm{nl}} = P_{uu}^{\mathrm{tot}}(1-\gamma_{us}(f))$$

where $\gamma_{us}(f)$ is the coherence function between the velocity fluctuation and the displacement signal. Figure 9 shows the (Wiener-filtered) amplitude evolution of the fluctuations at frequencies f_0 and $2f_0$. Three successive regions can be observed: an initial region of spatial exponential growth (where the linear regime is valid), a saturation region, and a region of decreasing amplitude. Without Wiener filtering, no exponential growth could be detected at frequency f_0. An increase of R reduces the region of spatial exponential growth, thus enhancing the turbulence transition.

IV. WEAK TURBULENCE: EVIDENCE OF DETERMINISTIC CHAOTIC FLOW

Velocity power spectra (Fig. 10 shows measurements taken at $X/D=15.36$, 21.12, and 25.44) reveal an exponential decrease in frequency of the peak amplitude at the excitation frequency and its harmonics, as well as of the broadband "noise." As the measuring probe moves downstream, an increase of the broadband noise level is noticed while the peaks remain at a constant amplitude value. An exponential decay of the broadband noise at high frequencies is recognized as a sufficient condition for the presence of "determinism" in a chaotic state.[23]

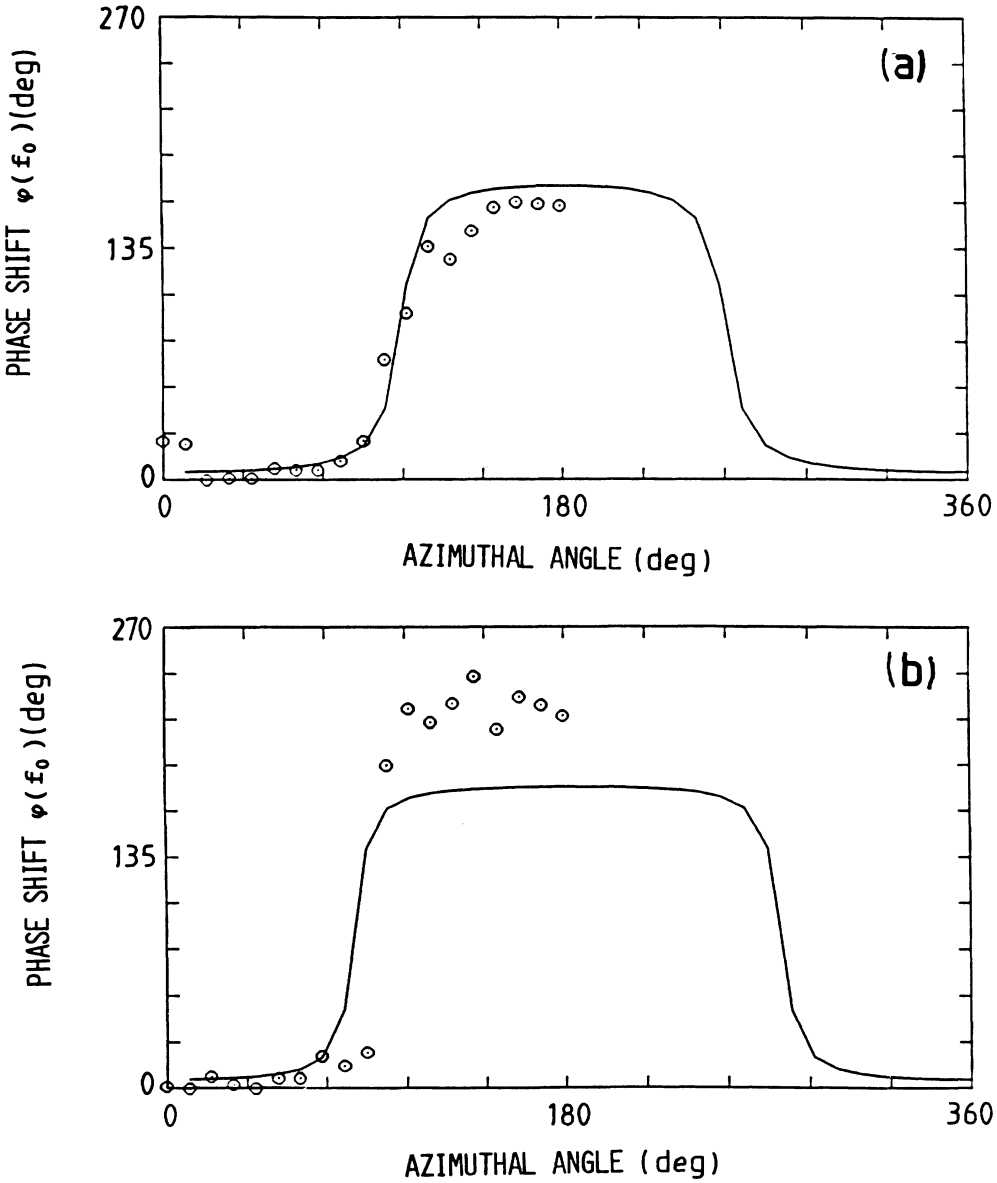

FIG. 7. Phase shift between the velocity fluctuations at frequency f_0 and the displacement signal, as a function of the azimuthal angle θ. Open circles: measured phase shift, azimuthal plane located at $X/D=16.0$ (a) and $X/D=19.2$ (b); radial probe position $r=1$ mm. Solid line: computed phase shift with (a) $\alpha_0=20°$ and $A_1=A_{-1}$, $A_1/A_0=1.6$, (b) $\alpha_0=140°$ and $A_1=A_{-1}$, $A_1/A_0=4.0$. Excitation frequency: $f_0=40$Hz with normalized rms velocity fluctuation $u/U\simeq 1.2\%$, and $R=395$. Cross-power spectra were averaged over 64 FFT's.

Therefore we conjecture the existence of an attractor whose dimension can be used as a statistical quantity to characterize the jet instability. We also raise the question of the downstream evolution of the attractor's dimensionality.

We shall first discuss the technique used to compute the attractor's dimension. We then show how this dimension correlates with the spatial coherence function introduced in Sec. III. Finally, in order to quantify the degree of chaos we present an evaluation of the Kolmogorov entropy.

Attractor Dimension. The probabilistic approach is used: one studies the scaling of the asymptotic probability density on the attractor when the size ϵ of the partition on the attractor decreases.[24] Obviously the multifractal nature of the attractor remains unknown until the complete spectrum of the generalized dimension D_q has been investigated.[25] We focused on the evaluation of the dimension of order 2, D_2; this choice is motivated mainly by the well-known difficulty of obtaining reliable results when dimensions are computed from experimental data. The analysis therefore requires a careful examination of

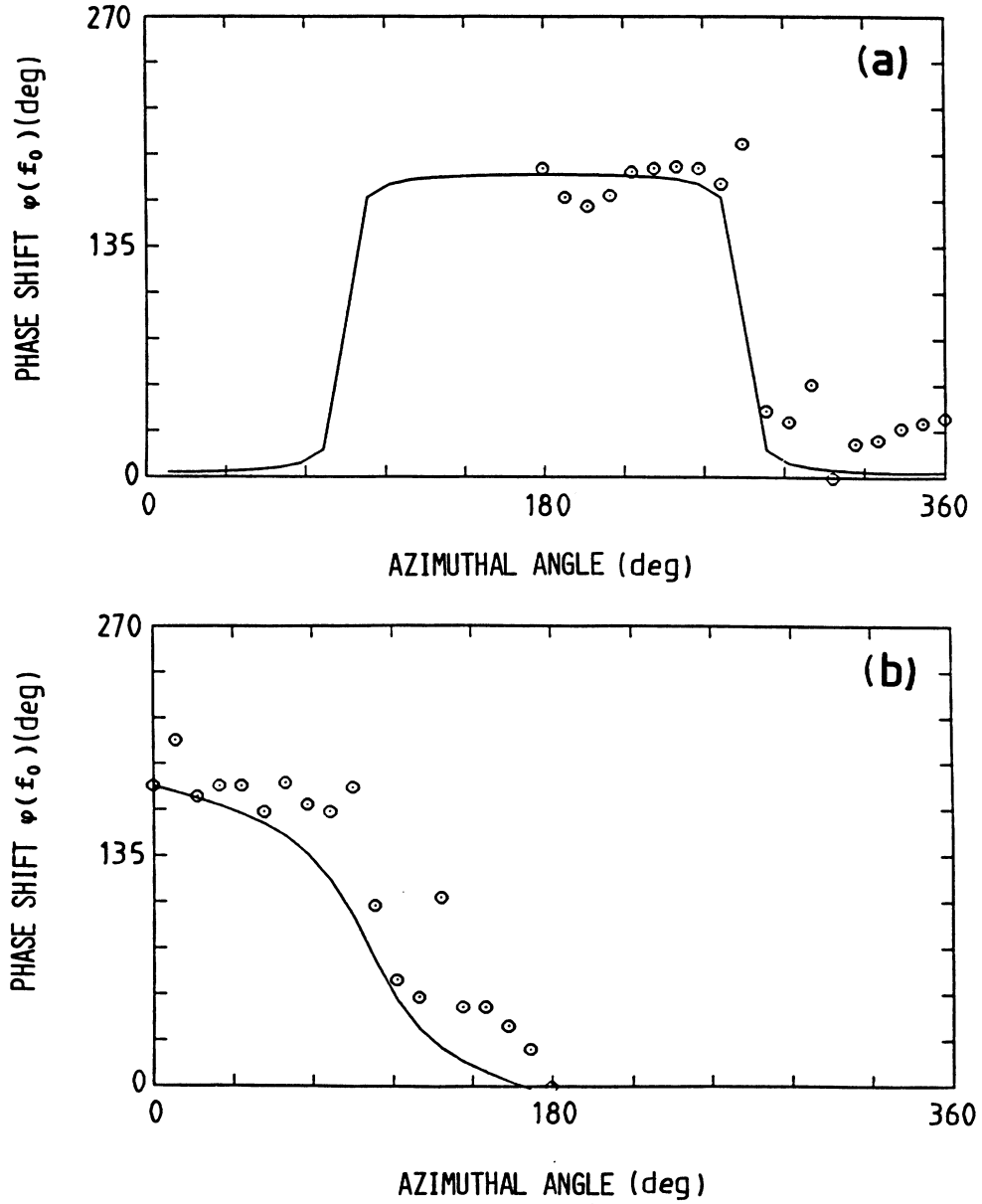

FIG. 8. Phase shift between the velocity fluctuations at frequency f_0 and the displacement signal, as a function of the azimuthal angle θ. (a) Open circles: present measurements, azimuthal plane located at $X/D=19.2$, radial probe position $r=1$ mm. Solid line: phase shift computed with $\alpha_0=90°$ and $A_1=A_{-1}$, $A_1/A_0=10.0$ Excitation frequency $f_0=40$ Hz, $u/U\simeq 0.9\%$, and $R=494$. (b) Open circles: present measurements, azimuthal plane located at $X/D=24$. Solid line: phase shift computed with $\alpha_0=10°$, $A_1/A_0=3.0$, and $A_{-1}/A_0=7.0$. Excitation frequency $f_0=40$ Hz, $u/U\simeq 1.1\%$, and $R=346$. Cross-power spectra were averaged over 64 FFT's.

the parameters influencing the dimension evaluation.

A lower bound to the second-order dimension D_2 is obtained from the correlation integral $C_d(\epsilon)$ defined as[26]—modified by Theiler's analysis[27]—

$$C_d(\epsilon)=\frac{1}{N_0(N_d-2w-1)} \times \sum_{i=1}^{N_0} \sum_{\substack{j=1 \\ j\notin(i-w,i+w)}}^{N_d} \Theta(\epsilon-|\mathbf{X}_i-\mathbf{X}_j|)$$

where $\Theta(\ )$ is the Heaviside function and ϵ is the radius of the hypersphere in phase space; $\mathbf{X}_i$ is the d-dimensional phase vector reconstructed from the single time series given by the velocity fluctuations, using the delay reconstruction technique,[28]

$$\mathbf{X}_i=[x(t),x(t+\tau),\ldots,x(t+(d-1)\tau)] ,$$

τ being the delay time. N_0 is the number of reference vectors in phase space and $N_d=N-(d\times p)$, where N is the total number of data points in the time series and p the time shift parameter. The correlation function represents the mean probability of finding two phase vectors on the attractor whose separation distance is less than or equal to ϵ.

With the delay reconstruction method it can be shown that[29]

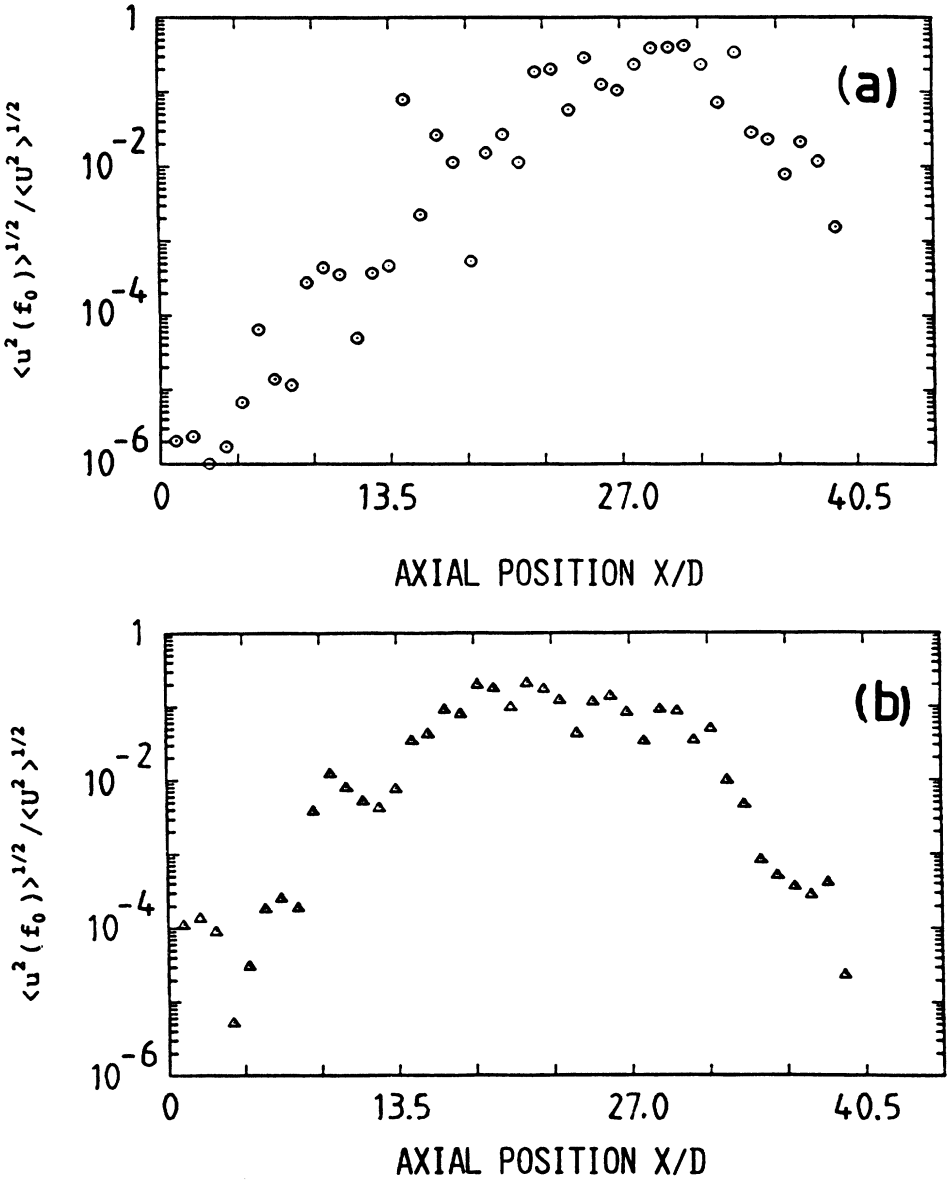

FIG. 9. Normalized rms Wiener-filtered velocity fluctuations as a function of the axial position X/D: (a) Component at the excitation frequency f_0, (b) first harmonic component. Excitation frequency $f_0=40$ Hz, $u/U\simeq 1.2\%$, and $R=426$. In the Wiener-filtering procedure, the coherence function is computed from cross spectra between the velocity fluctuations and the displacement signal, averaged over 24 FFT's.

$$C_d(\epsilon) \sim \epsilon^{\nu} e^{-H_{2,d}d\tau}$$

where ν is the correlation dimension, a lower bound to D_2. So, from a log-log plot of $C_d(\epsilon)$ versus ϵ, the correlation dimension is easily obtained in the scaling region of the correlation function if the embedding dimension satisfies $d \geq 2\nu+1$.[26] The order-2 correlation entropy is given by[29]

$$H_2 = \lim_{d \to \infty} H_{2,d}$$

where in the scaling region,

$$H_{2,d} = (1/k\tau) \log_{10}[C_d(\epsilon)/C_{d+k}(\epsilon)] ,$$

with k integer.

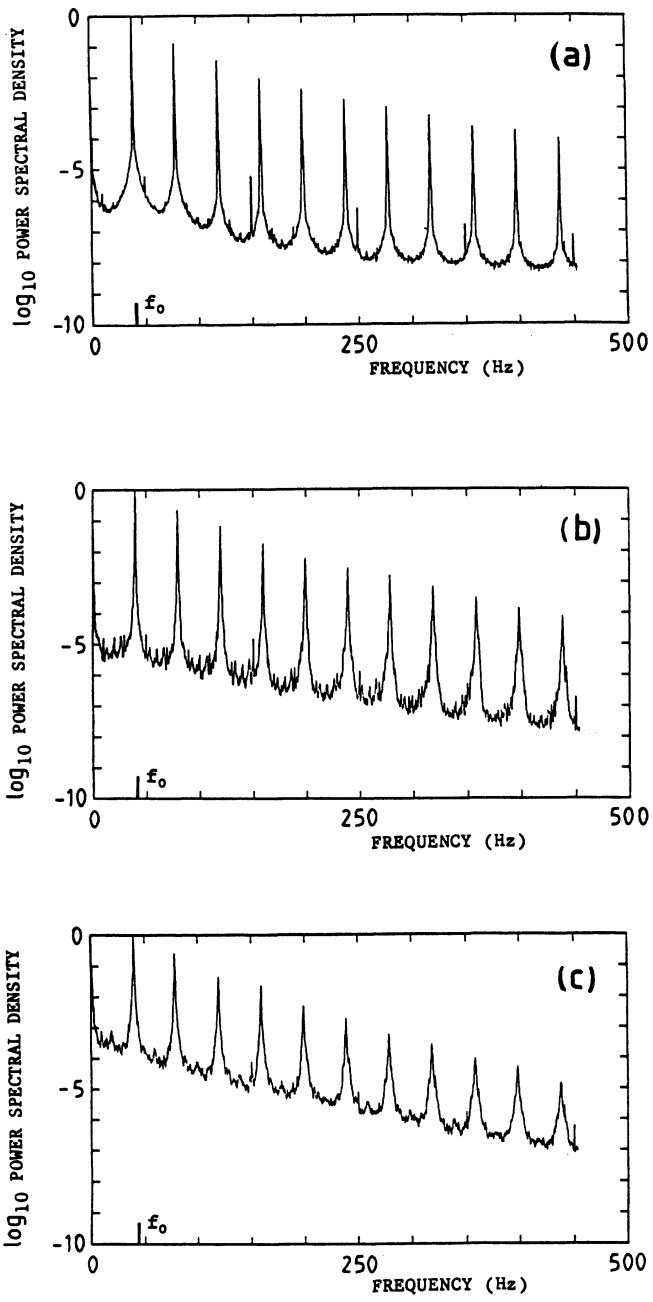

FIG. 10. Semilogarithmic plot of the normalized velocity power spectrum. Longitudinal position of probe $X/D=18.2$ (a), 21.1 (b), 24.0 (c); radial probe position $r=1$ mm. Each power spectrum is averaged over 48 FFT's of 2^{12} data points each with a frequency resolution $f=0.302$ Hz; a Hanning window is used. Excitation frequency $f_0=40$ Hz, normalized rms velocity fluctuation $u/U \simeq 0.95\%$ with $R=543$.

Many parameters enter the dimension evaluation when it is computed from a single time series. A correct choice of the time shift is crucial: $\tau = p\tau_s$, where p is the shift parameter and τ_s the sampling period. With an infinitely accurate time series, τ can be chosen arbitrarily. This is of course not the case in practice. In the literature, one finds the empirically established criterion $3 \leq T_0/\tau \leq 13-30$, where T_0 is the main pseudoperiodicity of the dynamics.[30,31] Recently, Fraser and Swinney[32] have proposed a method where the optimal time delay is given by the first minimum of the mutual information.[33] The mutual information is a measure of the dependence of two variables, say $x(t)$ and $x(t+\tau)$. If the mutual information is zero for a given τ, the system has lost in such a time interval the memory of its initial condition and consequently $x(t)$ and $x(t+\tau)$ are *independent.* By choosing, in the time series, variables spaced by a time interval τ, one selects the largest amount of information about the dynamics, and thus the phase vector is optimally reconstructed. Another method is to set the time delay equal to the time corresponding to the first zero of the autocorrelation function: in this case, the variables are orthogonal but not independent. For a highly periodic autocorrelation function, this gives $\tau \simeq T_0/4$ which is in the range of the empirical criterion.

Given $T=(d-1)p\tau_s$ the observation window (in the time series) used to reconstruct the d-dimensional phase vector, it is important to examine whether the dimension varies as a function of T. In fact, maintaining $T=T_0$, while increasing the dimension d of the embedding phase space can lead to an *apparent* saturation of the correlation dimension ν, thus giving a wrong estimate of the attractor dimensionality.[31] In our analysis, we consider that the *dynamics evolves on an attractor with a finite dimensional value if this value is T independent within a given range of T* (for small T, data in the observation window are too correlated: as a result, the reconstructed attractor concentrates along the diagonal of phase space, thus reducing its actual dimension; for too large values of T, data in the observation window are uncorrelated and consequently an artificial increase in the dimension follows).

The sampling period τ_s is also a critical parameter. Too small an acquisition period can lead to a completely wrong estimate of the dimension: for small τ_s a knee with slope $\simeq 1$ appears in the scaling region. Caputo[31] has shown that a large sampling period τ_s chosen between $T_0/7$ and $T_0/2$ can be considered as a satisfactory value. However, when the acquisition frequency is too low compared to the maximum frequency contained in the signal, Theiler's method must be used.[27] This method allows one

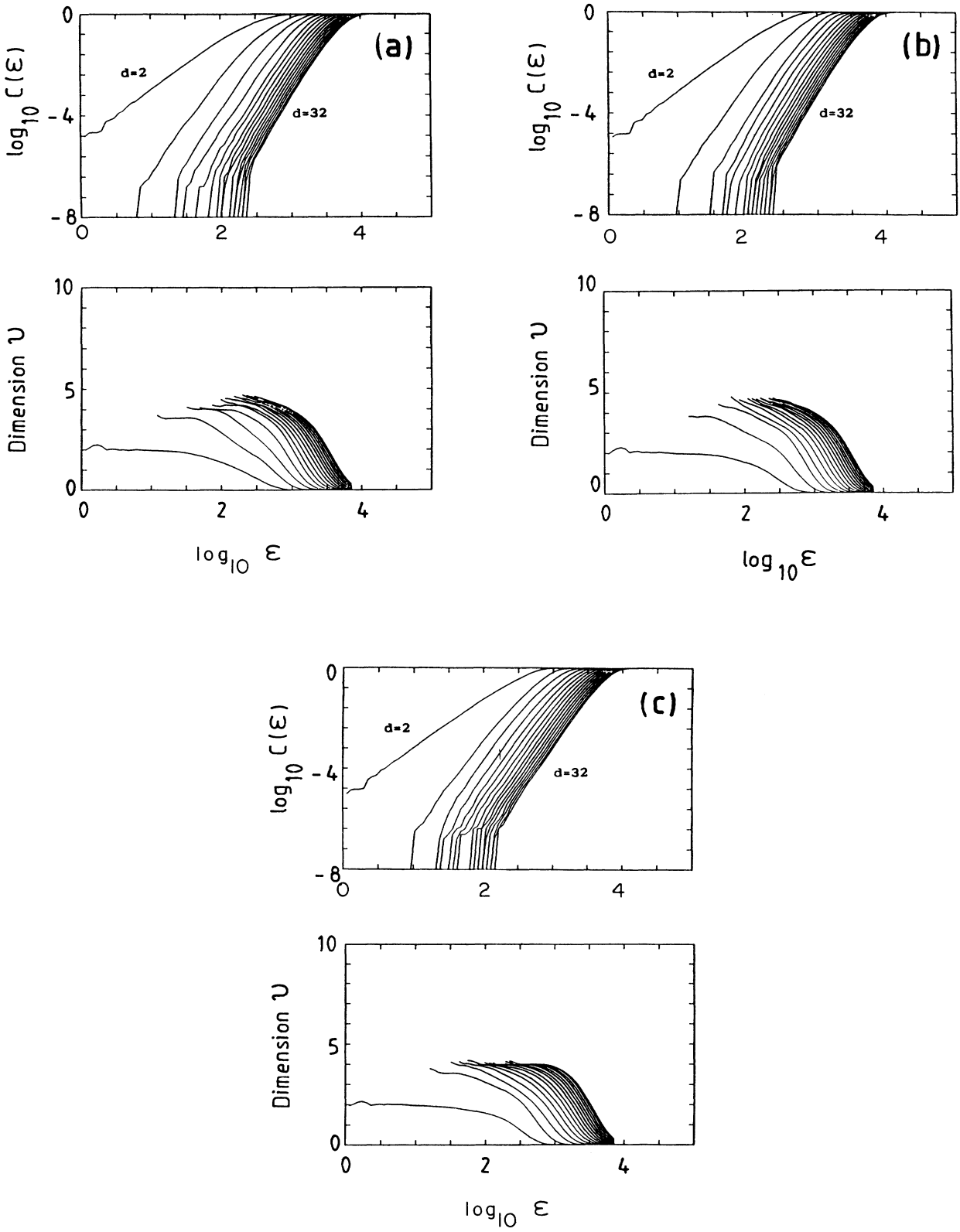

FIG. 11. Logarithm of the correlation function $C_d(\epsilon)$ and its slope computed by a linear regression over ten points, vs $\log_{10}\epsilon$, embedding dimension $d=2$ to $d=32$. (a) Shifting parameter $p=3$; cutoff parameter $w=800$; (b) $p=5$, $w=800$, (c) $p=8$, $w=500$. Number of data points $N=245\,760$, number of reference vectors $N_0=50$. Same experimental conditions as Fig. 10. Longitudinal position $X/D=21.1$, radial position $r=1$ mm.

to choose the acquisition frequency according to Shannon's criterion and independently of the attractor reconstruction constraints. The method introduces a cutoff parameter w generally chosen larger than τ_c, the autocorrelation time computed from the time series. The parameter w has the same effect as an increase of τ_s and reduces dramatically the knee in the correlation function plot by shifting the inflection point towards the large ϵ values—and outside the scaling region.

From the definition of the correlation function, use of the cutoff parameter w, when the separation distance between two phase vectors is evaluated, excludes those phase vectors whose index j is in the range $(i-w, i+w)$, where index i refers to the ith reference vector. Intuitively, this amounts to eliminating part of the trajectory centered on the ith reference vector to focus on the fractal structure of the attractor. Actually, this is equivalent to increasing the acquisition period, which artificially increases the distance between phase vectors along a reconstructed trajectory.

Practically, in the present analysis, the appropriate value of w is obtained by repeated trials until the knee in the correlation function disappears. This is a consequence of the very large autocorrelation time—and hence the difficulty of defining easily τ_c—in the transitional region because of the strong time periodicity in the velocity fluctuations. As an example, we mention that from velocity measurements at $X/D=19.68$, the inflection point in the correlation function plot disappears for $w \simeq 700$, which is equivalent to skipping about 23 orbits centered on each reference phase vector.

Experimental conditions. Since the reduced wavelengths obtained with different excitations follow the same spatial evolution along the jet axis (see Fig. 6), we have chosen to use a sinusoidal excitation with frequency $f_0=40$ Hz and normalized excitation intensity $u/U \simeq 0.95\%$ (with u the rms velocity fluctuation and U the mean exit velocity). The Reynolds number was set to 543, i.e., $(R-R_c)/R_c \simeq 13.3$. Velocity measurements were performed with the single hot-wire positioned at a radial position $r=1$ mm from the jet axis. The explored longitudinal region is between 4 and 30 diameters. We took 245 760 data points per position with an acquisition frequency $f_s=1237$ Hz using a low-pass filter set at 500 Hz. If the inverse of the excitation frequency is taken as the typical pseudoperiodicity of the dynamics, the measured attractor is roughly composed of 8000 revolutions.

Since the total observation time of the variable is fairly long ($\simeq 199$ sec/acquisition), we verified the stationarity—in the *weak sense*—of the velocity fluctuations by computing the first three moments. The run test method was used, which indicated a weak stationarity of the studied time series within a 90% confidence level (for the analysis, each record was subdivided into 20 to 40 time series).[18,34]

When computing the correlation function, by assuming the ergodicity of the attractor, we used $N_0=50$ reference vectors *randomly* distributed in the time series, which gave 12×10^6 computed correlations per embedding dimension. In the present analysis, we explored a large number of revolutions while the number of reference vectors was maintained at a fairly small value in order to reduce the computation time. In a previous study[35] the number of pseudorevolutions was only 262 and no slope saturation for increasing embedding dimensions could be observed when $\nu \geq 3$. The maximum explored embedding dimension was $d=32$ (for an evaluation of the Kolmogorov entropy, d was varied up to $d_{\max}=64$) since the Grassberger-Procaccia algorithm is known to give reliable results for correlation dimensions not exceeding 7–8 (see, e.g., Brandstater and Swinney[23]).

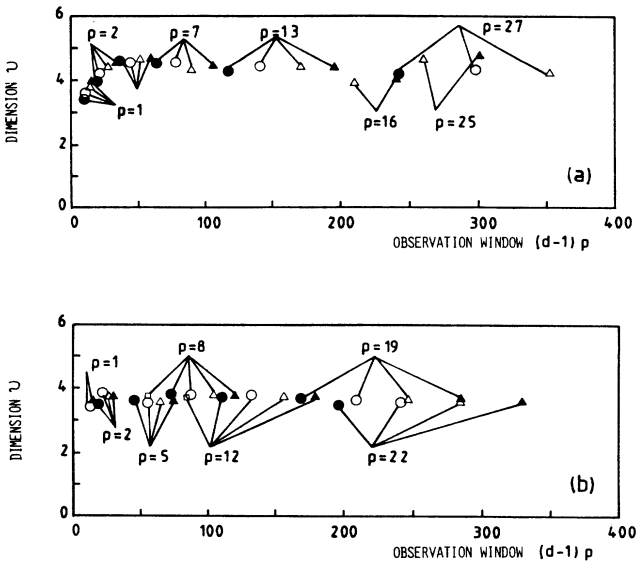

FIG. 12. Correlation dimension $\tilde{\nu}$ as a function of the observation window $(d-1)p$. Embedding dimension: $d=16$ (solid triangles), 14 (open triangles), 12 (solid and open circles), 10 (open squares). Longitudinal position: $X/D=16.8$ (a) $X/D=19.7$ (b); $N=245\,760$, $N_0=50$; same experimental conditions as Fig. 10.

Experimental results. The slope in the correlation plot, Fig. 11, is computed with a ten-point linear regression

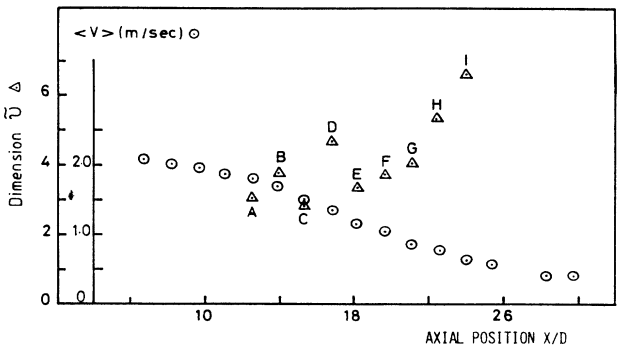

FIG. 13. Correlation dimension $\tilde{\nu}$ (triangles) and mean local velocity U (circles) as a function of the axial position X/D. Same experimental conditions as Fig. 10. It is to be noticed that from $X/D \simeq 20$ downward, the nonexcited jet is self-similar.

and the correlation dimension is obtained as the saturation value over a plateau corresponding to the scaling region. To evaluate the sensitivity of the correlation dimension to the reconstruction parameters, we plotted ν versus $(d-1)p$ for each time series. Figure 12(a) shows the behavior of ν for a time series recorded at $X/D=16.80$: ν first increases regularly for $(d-1)p<30$, then reaches a maximum for $30<(d-1)p<50$, and fluctuates slightly around a constant value for $(d-1)p>60$. Although the initial increase of ν for small values of $(d-1)p$ is less evident for the other time series [see, for example, Fig. 12(b)], the generally observed trend is a *plateau* value $\tilde{\nu}$ for $T_0/\tau_s \leq (d-1)p \leq (7 \text{ to } 13)T_0/\tau_s$.

In Fig. 13 we plot $\tilde{\nu}$ as well as the local mean velocity as a function of the axial position X/D. A continuous increase of $\tilde{\nu}$ is observed for $X/D \geq 18$. When $\tilde{\nu}$ exceeds 6, i.e., for $X/D>24$, no satisfactory saturation of the correlation function slope could be obtained in the scaling region. On the other hand, for $X/D \leq 12$, the extent of the scaling region was too small (because of the low-valued signal-to-noise ratio, $\leq 10^3$) to produce reliable results.

In order to validate our dimensionality computation, we correlated the spatial evolution of $\tilde{\nu}$ with the spatial coherence function computed between the velocity fluctuations and the displacement signal. Comparison of Figs. 13 and Fig. 14(a) shows that a decrease of the attractor dimension corresponds to an increase of the coherence function and vice versa. The presence of the

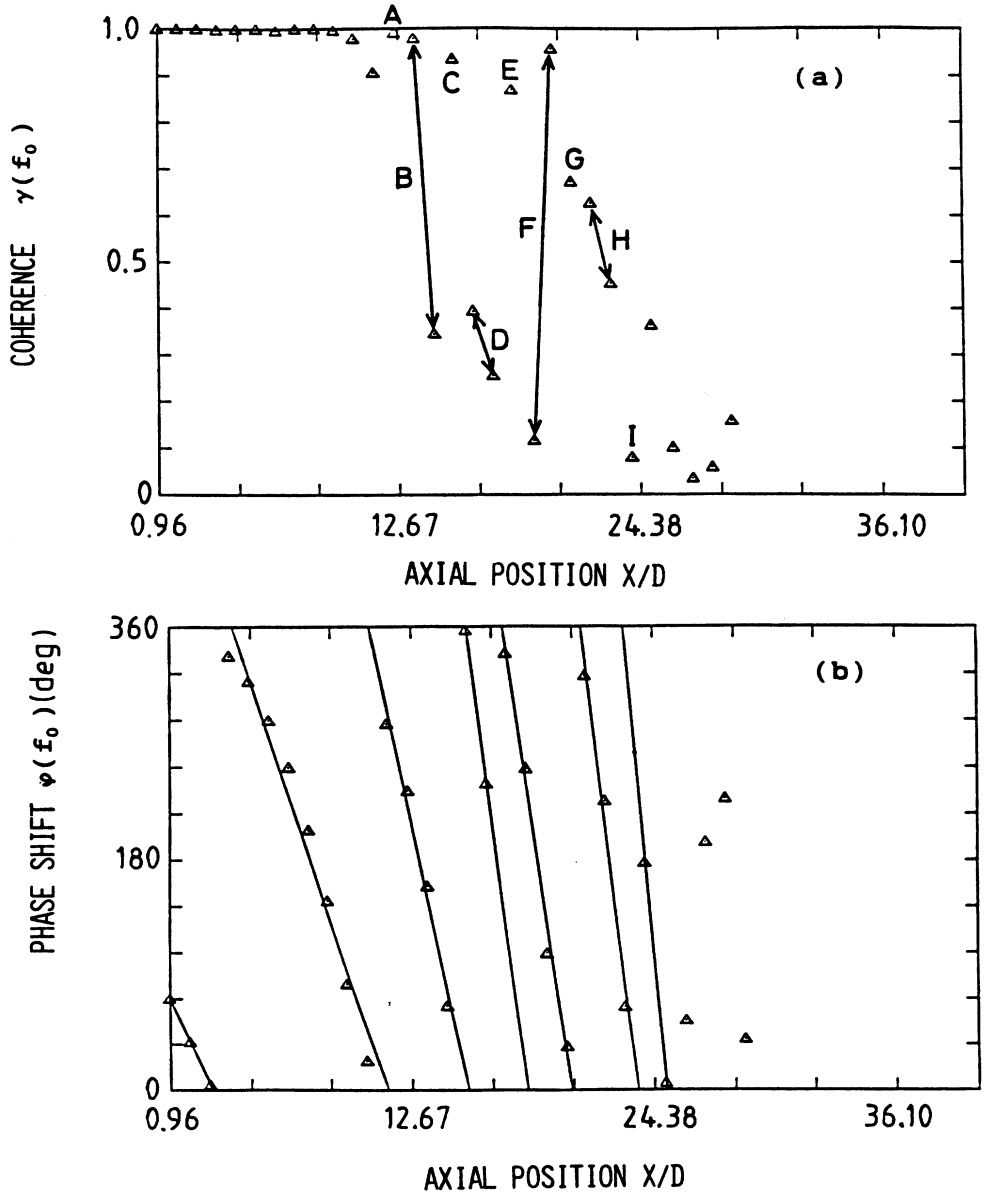

FIG. 14. The coherence function (a) and the phase shift (b) between the velocity fluctuation component at frequency f_0 and the displacement signal, as a function of the axial position X/D. The capital letters correspond to those of Fig. 13. A double-arrowed capital letter indicates the range within which the coherence function is expected to be. Each cross spectrum is averaged over 24 FFT's of 2^{11} points each. Same experimental conditions as given in caption of Fig. 10.

coherent structure can explain the low dimensionality of the attractor. On the other hand, a decrease in the coherence function can be attributed to a destabilization of the helical structure and therefore corresponds to an increase of the attractor dimension. The evolution of the spatial phase shift [Fig. 14(b)] indicates that the helical structure is still persistent even when the coherence is low valued. Notice that the coherence function was computed from several different time series obtained after a complete switch off of the excitation mechanism and of the flow; that the behavior of $\tilde{\nu}$ and $\gamma(f_0)$ is quite consistent is an indication of the presence of deterministic dynamics in the flow. Furthermore, it shows that the flow instability—in a statistical sense—is a well-reproducible phenomenon in space.

In Fig. 15 we present the normalized Wiener-filtered rms velocity fluctuations at frequency f_0 and $2f_0$ as a function of the axial position. The region where the attractor dimension increases continuously (Fig. 13) corresponds to the amplitude saturation region of the two modes (Fig. 15) (we conjecture the same trend for the higher harmonics). We evaluated the *pseudoentropy*[36] $H=(1/n)\sum_{i=1}^{n}\log_{10}p_i$, where p_i is the power of the velocity component at frequency f_i and n is the total number of frequency components chosen in the power spectrum. The pseudoentropy can be used to quantify the power spectrum as a measure of the growth of new modes in the dynamics: Fig. 16 shows that, in the region where the main peaks at f_0 and its harmonics are amplitude saturated (Fig. 15), a decrease in H comes from the growth of the broadband noise level (see Fig. 10), i.e., intermediate peaks fill in the valleys in the power spectrum. By

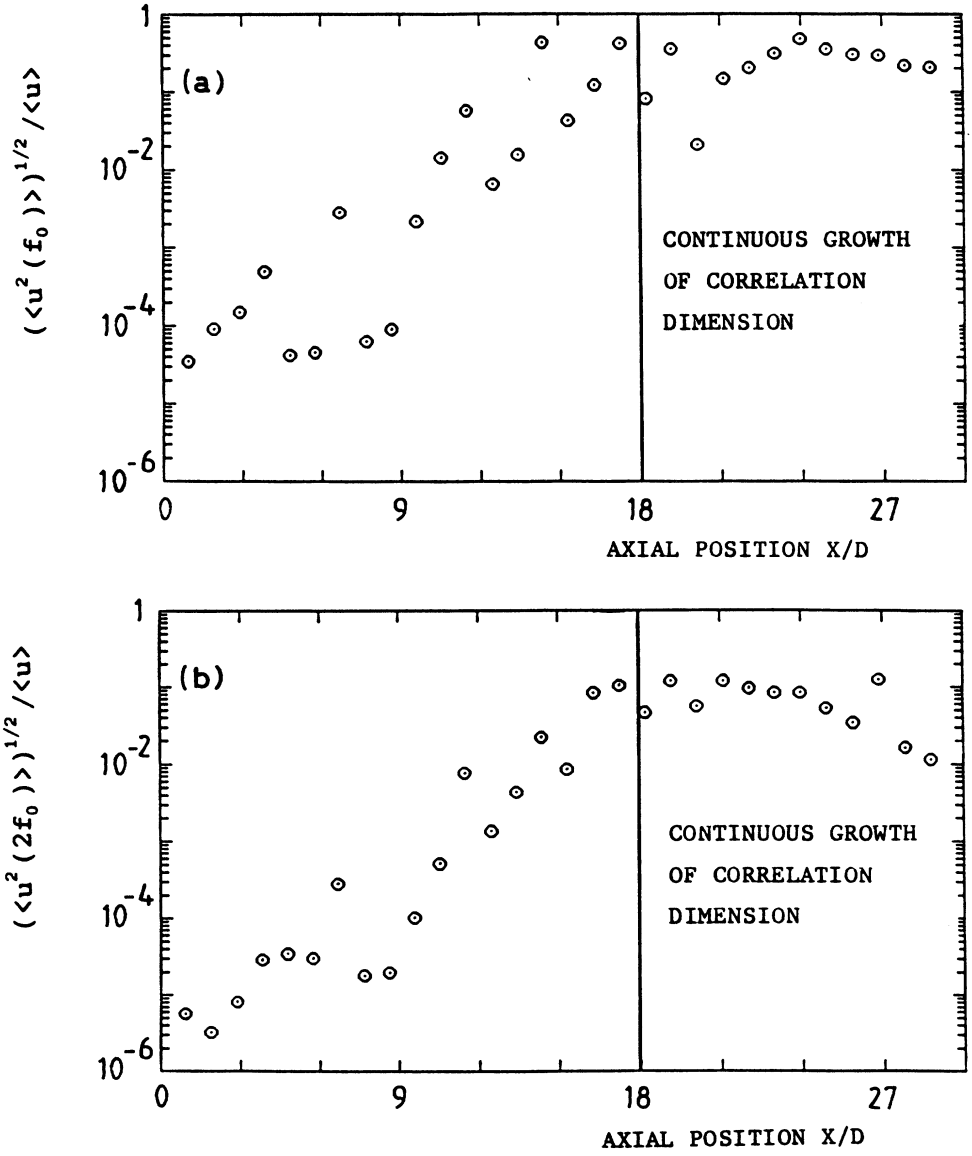

FIG. 15. Normalized rms Wiener-filtered velocity components as a function of X/D. (a) f_0 component, (b) $2f_0$ component. Same experimental conditions as for Fig. 10.

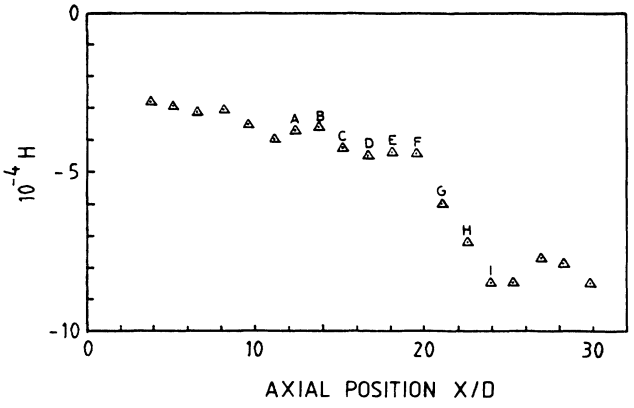

FIG. 16. Pseudoentropy H (see text) as a function of the axial position X/D. The pseudoentropy is computed over the frequency interval 0–450 Hz from power spectra averaged over 48 FFT's of 2^{13} points each. Capital letters correspond to those of Fig. 13. Notice that the large decrease of the pseudoentropy H from F to I corresponds to the continuous increase of the correlation dimension $\tilde{\nu}$ (Fig. 13).

comparison of these results with those of the dimensionality computation (Fig. 13) it appears that the increase of attractor dimension is to be related to the growth of the broadband noise level.

We estimated the Kolmogorov entropy by computing the second-order correlation entropy H_2. For increasing embedding dimension, d, the correlation curves are shifted in the log-log plane (Fig. 11) by a quantity $-H_{2,d}\tau d$ where $\tau=\tau_s p$. If the dynamics has a finite entropy, $H_{2,d}$ must converge asymptotically towards a finite value given by the second-order correlation entropy $H_2=\lim_{d\to\infty}H_{2,d}$ (for $\epsilon\to 0$). We conjectured that for finite embedding dimension, the following empirical relation holds:[37]

$$H_{2,d}=\frac{A}{d}+B$$

where A and B are constants; then in the limit $d\to\infty$, the second-order correlation entropy should be given by $H_2=B$. We tested the method with the McKay-Glass attractor; the value of H_2 so obtained is in agreement with Termonia's analysis;[38] see Fig. 17. We then applied the method to the weakly turbulent jet, using a time series measured at $X/D=18.24$. The results are given in Fig. 18. The maximum embedding dimension was set to $d=64$ and the phase-space dimension was increased with a step $\Delta d=2$. $H_{2,d}$ was averaged over a range $\Delta\epsilon$, where a well-defined plateau of the correlation dimension could be observed, i.e., $H_{2,d}=\langle H_{2,d}\rangle_{\Delta\epsilon}$. The smallest embedding dimension $d_{\min}$ used to establish the linear regression was such that for increasing $d\geq d_{\min}$, the plateau of the correlation dimension was always within the same range $\Delta\epsilon$. Caputo and Atten[29] have shown that the second-order correlation entropy depends on the observation window $T=(d-1)p\tau_s$ and that only for $T>6T_0-7T_0$, an asymptotic value could be obtained. In all our data reduction we verified this condition. Despite these precautions, the second-order correlation entropy was found to be very sensitive to small changes in the averaging interval $\Delta\epsilon$, as illustrated in Figs. 18(c) and 18(d). This sensitivity rules out the possibility of any valuable correlation between H_2 and the measured correlation dimension. Nevertheless, the finite value of H_2 confirms the existence of deterministic dynamics in the flow.

V. SPATIO-TEMPORAL TURBULENCE

It is known that large aspect ratio systems in their transitional regime are governed by spatio-temporal intermittency, where laminar spatially coherent regions are trapped between turbulent zones.[39] Such a behavior can be interpreted as a mechanism of mode competition whose strength increases with the nonlinearities. Consequently a local temporal analysis is not sufficient to describe the overall velocity fluctuating field and a dimensionality analysis performed from a single time series must be related to the flow dynamics in the neighborhood of the probing point. In an ideally accurate measurement, *every* point of the flow field contributes to the fluctuating dynamics at the measurement point. The *one-point* correlation dimension, computed from a local measurement, is thus an *extensive* quantity, depending on the "length" of the system. In order to define an *intensive* quantity—the *information density*, which represents, e.g., the number of degrees of freedom per unit length for a 1D flow—a *two-point correlation dimension* has been introduced by Pomeau.[40] This technique applies to homogeneous turbulent flow, and is based on the existence of a *characteristic length* over which two separated points in the flow are mutually dependent (the characteristic length is a function of the experimental resolution). Recent numerical simulations performed on a 1D coupled-map lattice[41] have shown that this characteristic length is comparable to the zero cross-correlation distance between two points and to the zero spatial mutual information between two points.

We tested the two-point correlation method in order to obtain the information density per unit length of the jet column. The two-point correlation function was computed from a reconstructed time series obtained by interleaving the velocity fluctuations taken at two separate points along the jet axis. No clear scaling region could be observed, which is most probably a consequence of the flow nonhomogeneity: large differences in the velocity fluctuations at the two points produce a *steplike* correlation function curve.

In a spatio-temporal flow, two points are spatially correlated if the time required for a disturbance to travel from one point to the other is smaller than the inverse of the largest Lyapunov exponent μ,[42] which represents the rate at which the information carried by the disturbance is lost. It is thus possible to define a spatial coherence length $\xi\equiv c/\mu$ where c is the transmission velocity of the information. A finite value of ξ characterizes an interaction range smaller than the typical length L of the sys-

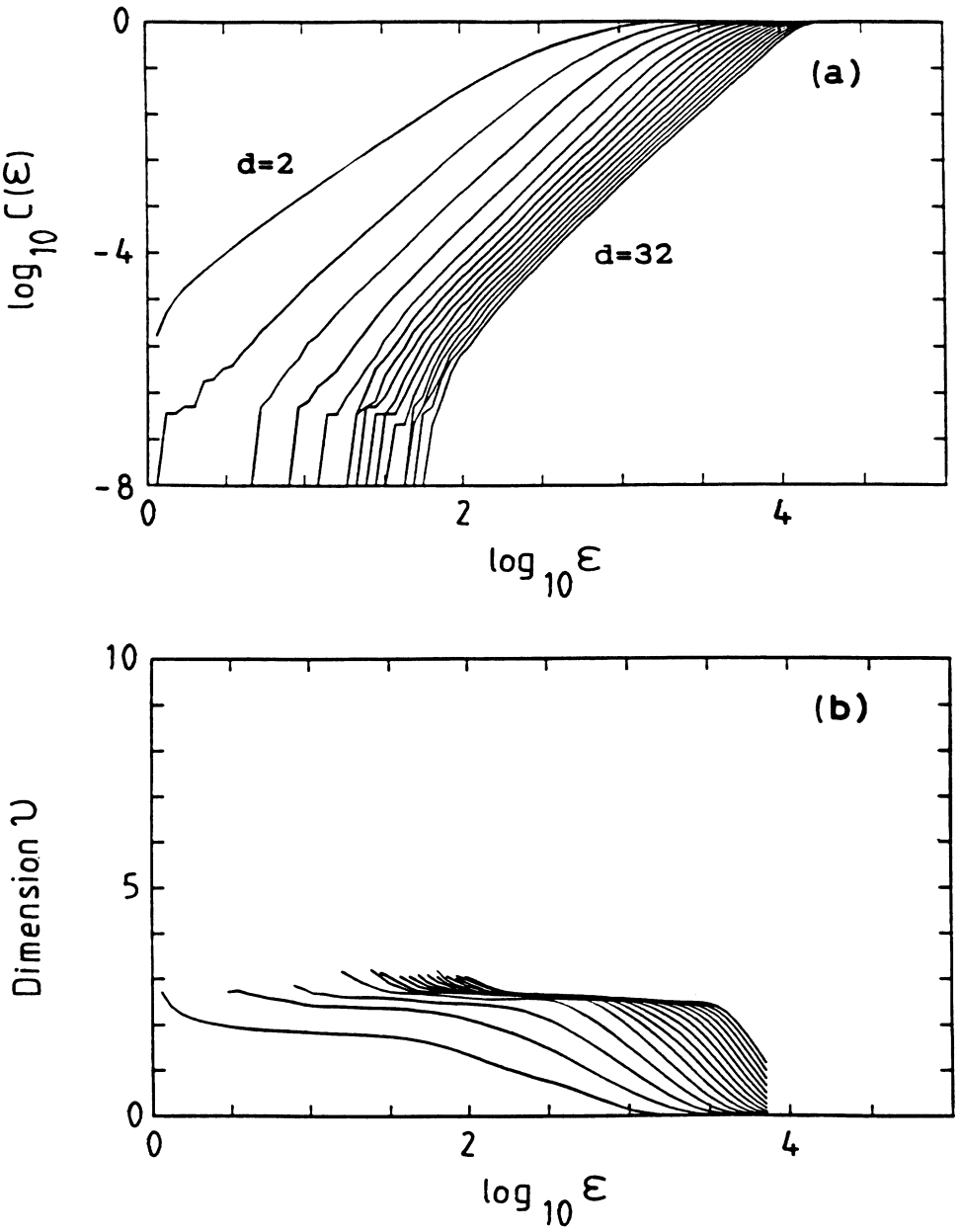

FIG. 17. Correlation function and entropy for the McKay-Glass equation (with time delay $s=30$). Log-log plot of $C_d(\epsilon)$ (a) and slope of $\log_{10}C_d(\epsilon)$ obtained by a linear regression computed over ten points (b). Number of data points: $N=42\,571$; number of reference vectors: $N_0=400$; shifting parameter: $p=3$; cutoff parameter: $w=1000$. Pseudoentropy $H^*_{2,d}$ as a function of $1/d$: (c) averaging interval: $2.45\leq\log_{10}\epsilon\leq 2.55$, value normalized by the time delay s: $H_2=(0.0084\pm0.0025)s^{-1}$; (d) averaging interval: $2.45\leq\log_{10}\epsilon\leq 2.65$, $H_2=(0.0088\pm0.0023)s^{-1}$.

tem, and so indicates the presence of chaotic dynamics over *local* length scales. For a given finite-valued ξ, the number of degrees of freedom is thus given by $(L/\xi)^d$ where d stands for the spatial dimension where the flow takes place. Because of the difficulty of computing accurate Lyapunov exponents from experimental time series, we define instead a *local* spatial correlation length based on the local phase speed and coherence,

$$\xi_{\rm loc}=f_0^{-1}c_{\rm ph}(f_0)\gamma(f_0)\ ,$$

where $c_{\rm ph}(f_0)$ is the phase speed of the disturbance at the excitation frequency f_0 and $\gamma(f_0)$, the local coherence at frequency f_0 (see Sec. III). The local phase speed is determined by measuring the phase shift $\theta(f_0)$ between two neighboring probes in the flow

$$c_{\rm ph}(f_0)=\frac{2\pi f_0\Delta x}{\theta(f_0)}$$

where Δx, the separation distance between the two

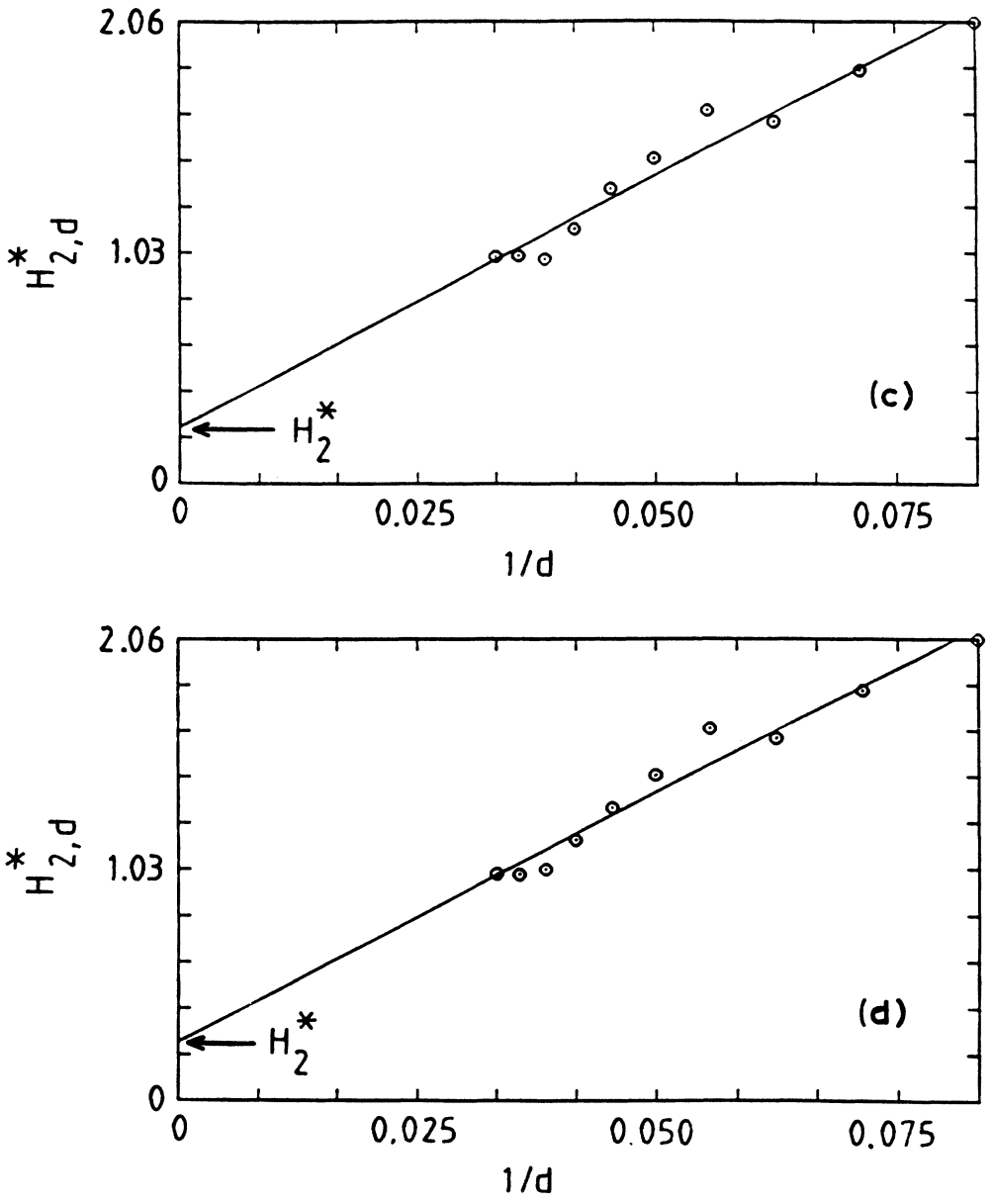

FIG. 17. (*Continued*).

probes, is much shorter than the mean wavelength. The phase shift and the coherence were evaluated from cross-power spectra averaged over 64 FFT's directly from the spectrum analyzer (HP 3582-A).

The behavior of the local correlation length as a function of the dimensionality is presented in Fig. 19. The experimental results show a linear behavior in the log-log plot, wherefrom a power law can be inferred:

$$\xi_{\text{loc}}=\beta\tilde{\nu}^{-\alpha}$$

where $\beta\simeq 1.82(m)$ and $\alpha\simeq 1.78$ (obtained by linear regression). Moreover, since the helical structure is still persistent even where $\tilde{\nu}\simeq 6$ we can assume that the flow remains one dimensional. The information density is thus given by

$$n=\frac{\tilde{\nu}}{\xi}=\beta^{-1}\tilde{\nu}^{1+\alpha}\ .$$

An analysis was performed along the same lines, introducing a *global* spatial correlation length, defined with the mean local velocity U and the coherence $\gamma(f_0)$ between the velocity fluctuations and the displacement signal. The same power law was found to hold with $\alpha\simeq 2.28$ and $\beta\simeq 4.2(m)$.

The measurements performed locally and globally (with respective distances between the probe and the reference of about 1 mm and over the whole range of the

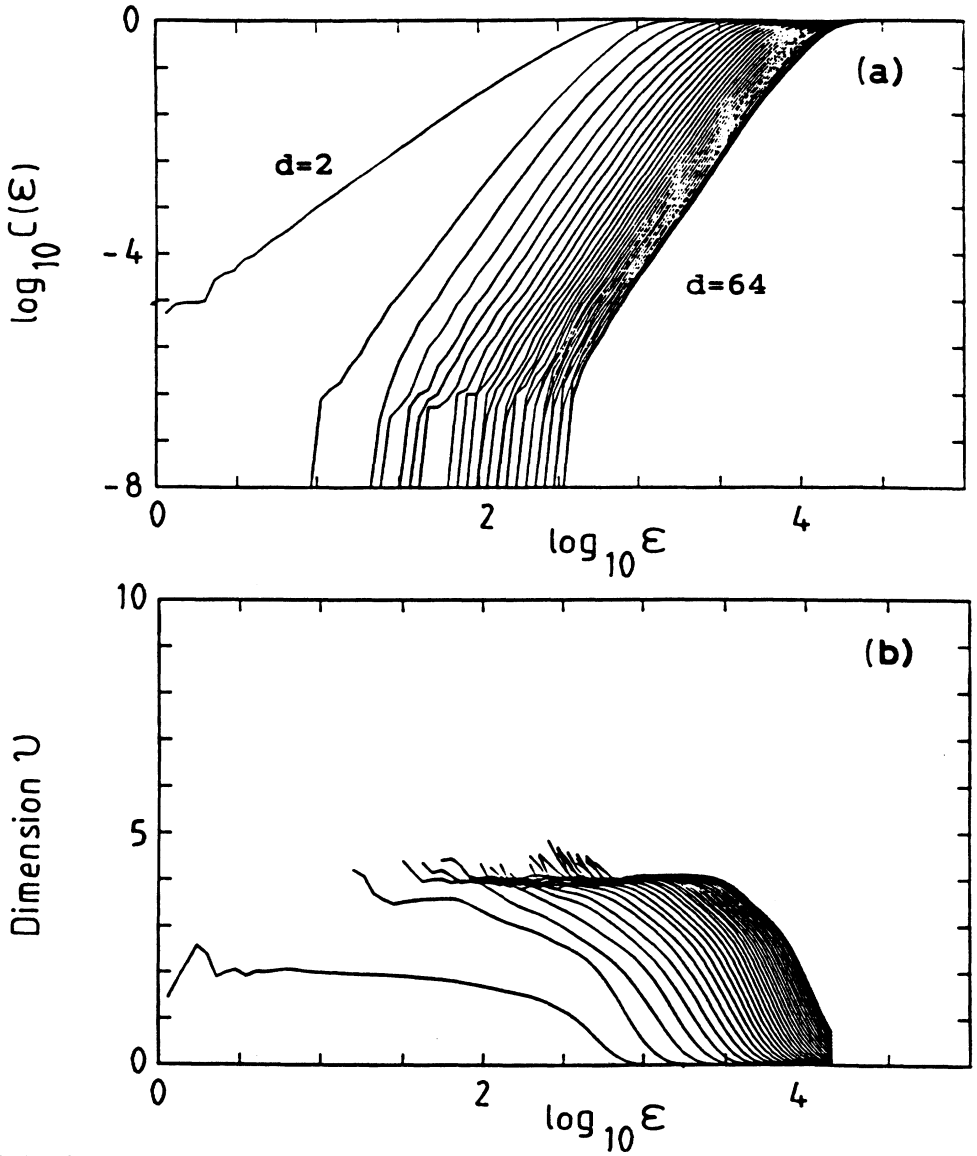

FIG. 18. Correlation function and entropy for the weakly turbulent jet (experimental conditions as for Fig. 10). Same as Fig. 17 but data from an experimental time series taken at $X/D=18.24$ with $N=245\,760$, $N_0=50$, $p=4$, $w=500$. The pseudoentropy $H^*_{2,d}$ is normalized by the excitation frequency $f_0=40$ Hz; (c) averaging interval: $2.75 \le \log_{10}\epsilon \le 3.00$, $H_2=(6.56\pm1.72)s^{-1}$; (d) averaging interval: $2.75 \le \log_{10}\epsilon \le 3.20$, $H_2=(1.80\pm1.36)s^{-1}$.

jet) yield correlation dimension exponents α that do not differ by more than 30%. From this observation, one can conjecture that the correlation dimension computed from a local time series is to be related to the flow dynamics over a local spatial correlation length. Furthermore, the phase speed and coherence were measured independently from the time series used for dimensionality computation; the fact that we obtain consistent results from independent data sources gives us confidence in the dimensionality analysis performed in the transition region.

VI. NONLINEAR QUADRATIC INTERACTIONS AND LONGITUDINAL EVOLUTION

As discussed in Sec. III, provided that the normalized velocity fluctuations do not exceed 2%, the linear approximation holds for an azimuthal mode decomposition of the f_0 component. We now analyze the nonlinear process of generation of the harmonic components along the jet axis and the mechanism which is responsible—partly at least—for the growth of the noise level in the power spectrum. Our analysis relies upon the *bicoherence function* which quantifies *quadratic nonlinearities* between modes.[43] The bicoherence function has been used extensively by Miksad *et al.*[44] to study free turbulent transition in a 2D mixing layer. In the amplitude saturation region of the main peaks, these authors have shown that the growth of the noise level can be explained through a cross-interaction mechanism between sidebands. This nonlinear interaction transfers energy into the empty valleys of the power spectrum which are located between the main peaks, and shifts the power to low frequencies.

As long as one considers a process consisting of a

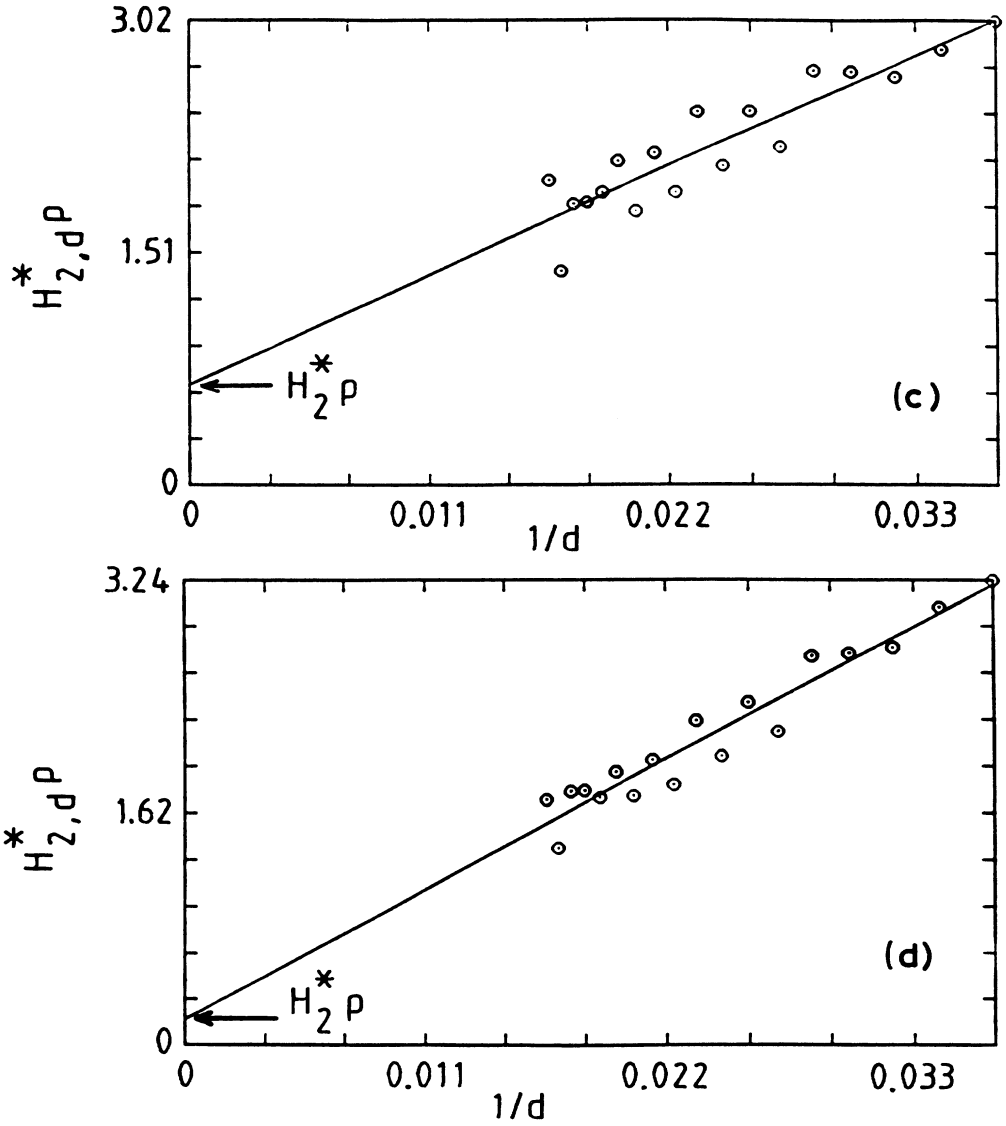

FIG. 18. (*Continued*).

linear superposition of independent modes, the (second-order) power spectrum is sufficient to describe the process. However, second-order power spectra are insufficient for a correct description of processes dominated by nonlinear interactions, due to the loss of phase information. In fact, in a nonlinear process, a mode can be generated through a nonlinear interaction between modes, in which case the phase of such mode cannot vary randomly as for a self-generated mode.

Polyspectra of order larger than 2 do not "lose" the phase coherence between modes and therefore can be used to describe nonlinear processes. In particular, the cross bispectrum can be used to evaluate the quadratic transfer function in a nonlinear process[45] as can the coherence function in a linear process. Here we consider the self-bispectrum which is the 2D Fourier transform of the third-order moment $R_{xxx}(\tau_1,\tau_2)=E[x(t)x(t+\tau_1)x(t+\tau_2)]$, where $x(t)$ is a weakly stationary random variable, at least up to order 3,[46]

$$B(f_1,f_2)=\int\int_{-\infty}^{\infty} R_{xxx}(\tau_1,\tau_2)e^{2\pi i(f_1\tau_1+f_2\tau_2)}d\tau_1 d\tau_2 .$$

By setting $\tau_1=\tau_2=0$ and taking the inverse Fourier transform, we note that $B(f_1,f_2)$ represents the contribution of the frequency components f_1 and f_2 to the simple third-order moment $E[x^3(t)]$.

For a three-wave resonant process where the resonance frequency relation holds $f_1+f_2=f_{1+2}$ (we assume also colinear and nondispersive waves), Kim and Powers have shown that, provided $x(t)$ is stationary and has a zero mean value,[43]

$$E[X_1X_2X^*_{1+2}]=B(f_1,f_2)$$

where $E[\ ]$ is the expectation value of the product of the Fourier amplitudes X_i of $x(t)$ at frequency f_i. From the relation given above we see that if the three modes are independent, the ensemble average vanishes because of the noncoherence of the phase between the modes.

The bicoherence is the normalized bispectrum

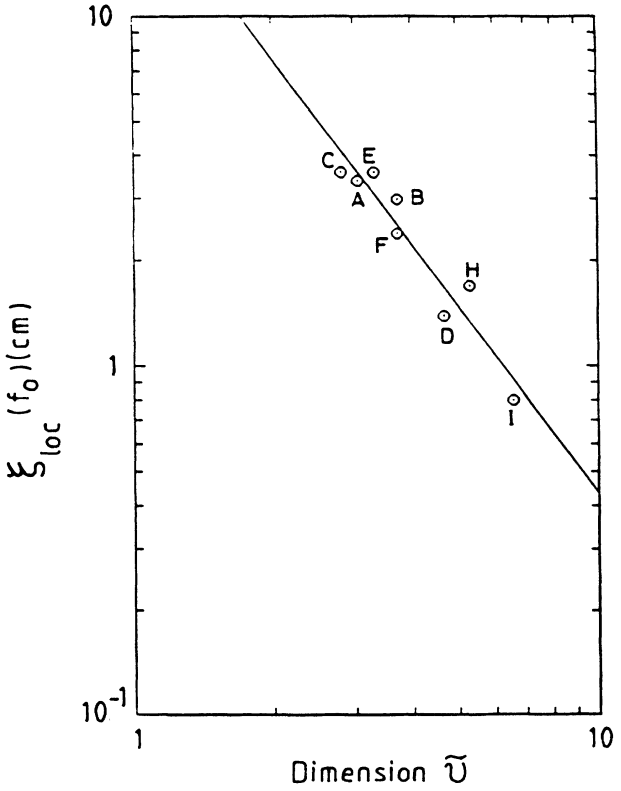

FIG. 19. Local correlation length as a function of the (one-point) correlation dimension $\tilde{\nu}$. Capital letters refer to those of Fig. 13; point G was eliminated in the linear regression because of too large an error bar with corresponding value of the phase speed at frequency f_0.

$$b(f_1,f_2)=\frac{\|E[X_1X_2X^*_{1+2}]\|^2}{E[\|X_1X_2^*\|^2]E[\|X_{1+2}\|^2]};\quad 0\le b\le 1\ .$$

When $b(f_1,f_2)=1$, the wave at frequency f_{1+2} is generated from a quadratic interaction between f_1 and f_2 waves, while when $b(f_1,f_2)=0$, the three waves are independent. The bispectrum is evaluated through the third-order periodogram

$$\langle B(f_1,f_2)\rangle=\frac{1}{M}\sum_{j=1}^{M}X_1^jX_2^jX_{1+2}^{j*}$$

where X_i is the ith Fourier amplitude computed over a time series of length $T_j=T/M$, T being the total observation time. The ensemble average was taken over $M=480$ fast-Fourier transforms of 512 points each, with a frequency resolution $\Delta f=2.4$ Hz. The value of M was chosen sufficiently large to ensure good convergence of the bicoherence estimator. For all the present results, the maximum width of the bicoherence fluctuation interval, observed for $M\ge 285$, is smaller than 0.1.

In a quadratic interaction process, a mode can arise from a *sum interaction* $B(f_1,f_2)$ or from a *difference interaction* $B(-f_1,f_2)$.[43] In our analysis we focused on sum interactions between modes. In order to evaluate the quadratic nonlinearities between the main peaks we exploited the same time series as used in Sec. V. In Fig. 20

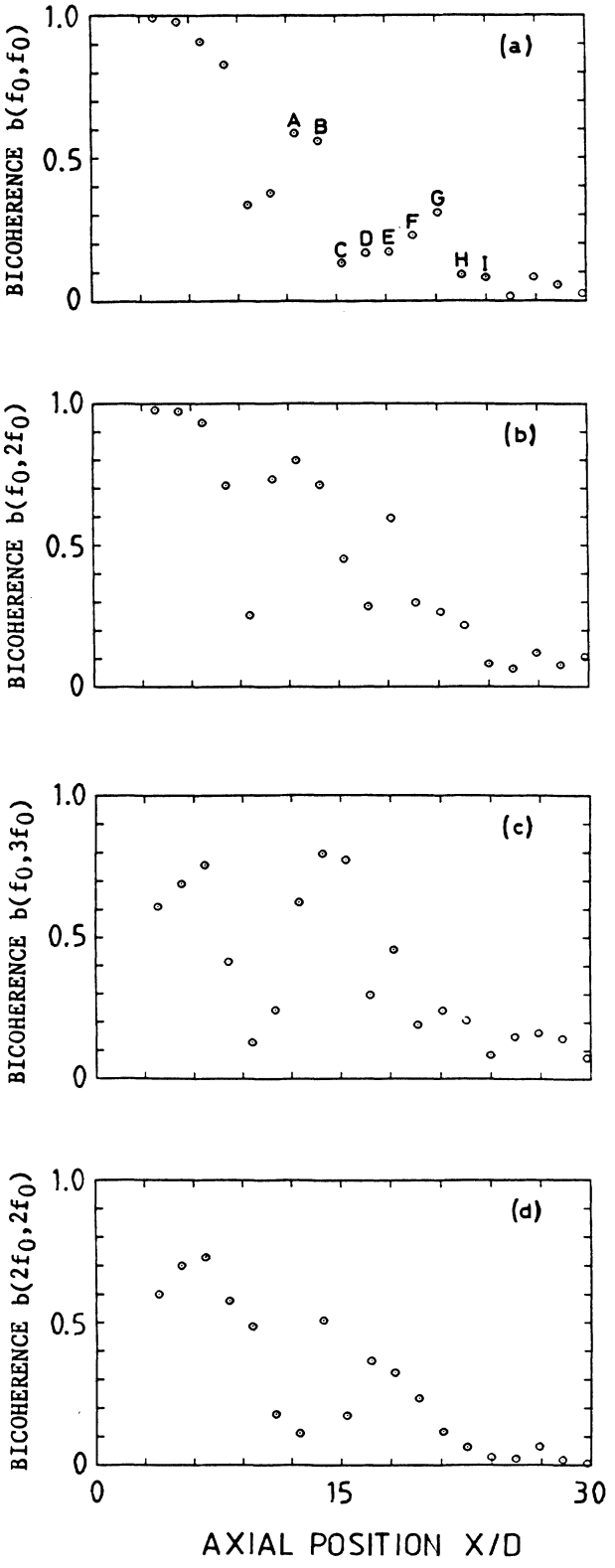

FIG. 20. Bicoherence as a function of the axial position for a quadratic interaction between modes: (f_0,f_0) (a), $(f_0,2f_0)$ (b), $(f_0,3f_0)$ (c), $(2f_0,2f_0)$ (d). The bicoherence is evaluated over 480 FFT's of 512 points each. Capital letters refer to those of Fig. 13; same experimental conditions as for Fig. 10.

we show the bicoherence as a function of the axial position, for sum interactions between modes (f_0,f_0), $(f_0,2f_0)$, $(f_0,3f_0)$, and $(2f_0,2f_0)$, respectively. We observe that in the region $X/D \leq 10$ where the pseudo entropy H decreases slightly (Fig. 16) and where the modes f_0 and $2f_0$ have a spatial exponential growth (Fig. 15), the bicoherence is high valued. In the amplitude saturation region of the main modes, $X/D \geq 18$ (Fig. 15) where H decreases abruptly (Fig. 16), the bicoherence is low valued. A low bicoherence is an indication of weak quadratic coupling and therefore of poor energy exchange between modes, which prevents amplitude growth.

From bicoherence isovalue plots (not shown) in the frequency plane (f_l,f_k), we observed, for increasing downstream positions, (i) an increase of the number of quadratic coupled modes, and (ii) a broadening of the isovalue regions around these main modes when they saturate in amplitude. More precisely, for a sum interaction, the bicoherence isovalue contour in the plane (f_l,f_k) coincides partly with the line $f_l+f_k=nf_0+\delta$ (n, integer), where the mode $(nf_0+\delta)$ is located in a valley of the power spectrum, between the main peak at f_0 and its harmonics. This shows that the sum interaction process, in the amplitude saturation region, is between $lf_0+\mu$ and $kf_0+\rho$ modes, with $l+k=n$ and $\mu+\rho=\delta$. This mechanism which corresponds to a quadratic cross interaction between power spectrum lobes, is similar to the one observed by Miksad *et al.*[44] and seems to be responsible for the broadband noise growth in the power spectrum.

The attractor dimension was found to grow in the mode amplitude saturation region (see Figs. 13 and 15); but in this region the quadratic coupling between the main modes is weak (see Fig. 20). Consequently, no relationship could be deduced between the longitudinal evolution of the bicoherence and the correlation dimension. This observation corroborates that the correlation dimension correlates best with the local *linear* correlation length, as Fig. 19 shows, rather than with a "nonlinear" correlation length based, for example, on the bicoherence function $b(f_0,f_0)$.

VII. SUMMARY

We studied the transition to turbulence in an open, axisymmetric flow far from the critical threshold. We first analyzed the spatial development of the jet instability in the regime of small fluctuations; we found that in this regime (i) the jet is viscously unstable and (ii) the simple helical mode is the most unstable mode in agreement with the linear spatial viscous stability analysis.

We showed that, in the transitional region where the helical mode is amplitude saturated, the instability can be described by a low-dimensional chaotic attractor. This low value is a consequence of the persistence of the helical mode as evidenced by the power law between the spatial correlation length and the attractor dimension. Our experimental results demonstrate that in open systems a one-point dimension computation characterizes *locally* the flow instability only on a local range. Despite the regular increase of the correlation dimension $\bar{\nu}$ (Fig. 13), the irregular downstream decrease of the correlation length ξ (Fig. 19) indicates that the dynamics in the jet should be nonuniform, which is possibly a consequence of a local relaminarization of the flow. Although no accurate evaluation of the entropy could be obtained, the finite nonzero value of H_2 appears as a clear indication of the presence of deterministic chaos in the flow.

Finally we notice that the longitudinal evolution of the helical coherent structure bears striking analogy with recent numerical simulations by Deissler[47] for a 1D Ginzburg-Landau equation with a *convective* term. In the presence of external random noise, the convective instability sequence is the following: (i) a linear domain where, according to the marginal stability curve, the noise is selected and amplified to generate spatially growing waves; (ii) a transitional region where nonlinearities are important and where amplitude saturation of the waves occurs; and (iii) a turbulent zone dominated by *local* nonlinearities (no correlation of the fluctuations with external noise).

ACKNOWLEDGMENTS

We wish to thank D. Olivari for fruitful discussions and M. Favre-Marinet and U. Frisch for valuable comments. One of us (J.P.B.) acknowledges support by the Fonds National de la Recherche Scientifique (FNRS, Belgium). This research was carried out at the von Karman Institute for Fluid Dynamics in collaboration with the Groupe de Physique Non-Linéaire et Mécanique Statistique at the Université Libre de Bruxelles.

*Address to which all correspondence should be sent.

[1]B. Malraison, P. Atten, P. Bergé, and M. Dubois, J. Phys. (Paris) Lett. **44**, 897 (1983); M. Dubois and P. Bergé, Phys. Scr. **33**, 159 (1986); M. Giglio, S. Musazzi, and U. Perini, Phys. Rev. Lett. **53**, 2402 (1984).

[2]R. W. Walden, P. Kolodner, A. Passner, and C. M. Surko, Phys. Rev. Lett. **55**, 496 (1985).

[3]F. H. Busse, Rep. Prog. Phys. **41**, 1930 (1978); J. E. Wesfreid, in *Cellular Structures and Instabilities,* edited by J. E. Wesfreid and S. Zaleski (Springer, Berlin, 1984).

[4]F. Helsot, B. Castaing, and A. Libchaber, Phys. Rev. A **36**, 5870 (1987).

[5]A. K. M. F. Hussain, J. Fluid Mech. **173**, 303 (1986).

[6]C. S. Subramamiam, S. Rajagopolan, R. A. Antonia, and A. J. Chambers, J. Fluid Mech. **123**, 335 (1982).

[7]P. Coullet, in *Non-Linear Phenomena in Physics,* edited by F. Claro (Springer-Verlag, Berlin, 1985); P. Manneville, Phys. Rep. **103**, 107 (1984).

[8]P. Bergé and M. Dubois, Contemp. Phys. **25**, 535 (1984).

[9]M. Provansal, C. Mathis, and L. Boyer, J. Fluid Mech. **182**, 1 (1987).

[10]C. X. W. Tam, J. Sound Vib. **105**, 169 (1986).

[11]G. K. Batchelor and A. E. Gill, J. Fluid Mech. **14**, 529 (1962).
[12]H. Schlichting, *Boundary Layer Theory* (McGraw-Hill, New York, 1979).
[13]W. A. Bell, AIAA J. **21**, 714 (1983).
[14]G. W. Rankin, K. Sridhar, M. Arulraja, and K. R. Kumar, J. Fluid Mech. **133**, 217 (1983).
[15]P. J. Morris, J. Fluid Mech. **77**, 511 (1976).
[16]M. Lessen and P. J. Singh, J. Fluid Mech. **60**, 433 (1973).
[17]B. W. Miksad, J. Fluid Mech. **56**, 695 (1972); **59**, 1 (1973).
[18]J. S. Bendat and A. G. Piersol, *Random Data: Analysis and Measurement Procedures* (Wiley-Interscience, New York, 1971).
[19]J. S. Bendat, J. Sound Vib. **59**, 405 (1978).
[20]J. Cohen and I. Wygnanski, J. Fluid Mech. **176**, 221 (1987).
[21]G. L. Morrison and D. X. McLaughlin, AIAA J. **18**, 793 (1980); T. R. Troutt and D. X. McLaughlin, J. Fluid Mech. **116**, 123 (1982).
[22]L. H. Koopmans, *The Spectral Analysis of Time Series* (Academic, New York, 1974); P. Caperan and A. Alemany, J. Mec. Theor. Appl. **4**, 175 (1985).
[23]D. Sieti and W. Horsthemke, Phys. Rev. A **35**, 2276 (1987); A. Brandstater and H. L. Swinney, *ibid.* **35**, 2207 (1987).
[24]J. D. Farmer, E. Ott, and J. A. Yorke, Physica D **7**, 153 (1983).
[25]P. Grassberger, Phys. Lett. **97A**, 227 (1983); S. Sato, M. Sano, and Y. Sawada, Prog. Theor. Phys. **77**, 1 (1987).
[26]P. Grassberger and I. Procaccia, Physica D **9**, 189 (1983); Phys. Rev. Lett. **50**, 346 (1983).
[27]J. Theiler, Phys. Rev. A **34**, 2427 (1986).
[28]F. Takens, in *Proceedings of the Warwick Symposium,* Vol. 898 of *Lecture Notes in Mathematics,* edited by D. Rand and B. S. Young (Springer, Berlin, 1981).
[29]P. Grassberger and I. Procaccia, Phys. Rev. A **28**, 2591 (1983); Physica D **13**, 34 (1984); J. G. Caputo and P. Atten, Phys. Rev. A **35**, 1311 (1987).
[30]A. Babloyantz and A. Destexhe, Proc. Natl. Acad. Sci. U.S.A. **83**, 3513 (1986); S. Martin, H. Leber, and W. Maitienssen, Phys. Rev. Lett. **53**, 303 (1984).
[31]J. G. Caputo, Ph.D. thesis, Grenoble, 1986; J. G. Caputo, B. Malraison and P. Atten, in *Proceedings of the Workshop Dimension and Entropies in Chaotic Systems,* edited by G. Mayer-Kress (Springer-Verlag, Berlin, 1986).
[32]A. M. Fraser and H. L. Swinney, Phys. Rev. A **33**, 1134 (1986).
[33]B. Pompe and R. W. Leven, Phys. Scr. **34**, 8 (1986); B. Pompe, J. Kruscha, and R. W. Leven, Z. Naturforsch., Teil A **41**, 801 (1986).
[34]M. Ceschia, R. Garfagnini, A. Lavenia, and E. Toppano, Nuovo Cimento C **9**, 859 (1986).
[35]M. Bonetti, R. Meynart, J. P. Boon, and D. Olivari, Phys. Rev. Lett. **55**, 492 (1985).
[36]A. Laffon, A. Rossi, and C. Vidal, J. Phys. (Paris) **44**, 505 (1983).
[37]J. P. Boon and M. Bonetti, in *Société Française de Physique,* edited by M. Le Bellac (Edition de Physique, Paris, 1985); T. Miura and T. Xai, J. Phys. Soc. Jpn. **55**, 2562 (1986).
[38]Y. Termonia, Phys. Rev. A **29**, 1612 (1984).
[39]P. Manneville, in *AGARD Report No. 755* (Nato, Paris, 1987); H. Chaté and P. Manneville, Phys. Rev. Lett. **58**, 112 (1987); H. Chaté (private communication).
[40]Y. Pomeau, C. R. Acad. Sci. Paris, **300**, Série **II(7)**, 239 (1985).
[41]G. Mayer-Kress and T. Kurz, Complex, Syst. **1**, 821 (1987).
[42]D. R. Rasmussen and T. Bohr, Phys. Lett. A **125**, 107 (1987); G. Grinstein, J. Stat. Phys. **5**, 803 (1988).
[43]Y. C. Kim and E. J. Powers, IEEE Trans. Plasma Sci. **7**, 120 (1979).
[44]R. W. Miksad, and F. L. Jones, and E. J. Powers, Phys. Fluids **26**, 1402 (1983).
[45]C. P. Ritz and E. J. Powers, Physica D **20**, 320 (1986).
[46]M. B. Priestley, *Spectral Analysis and Time Series* (Academic, London, 1981); T. Subba Rao and M. M. Gabr, *An Introduction to Bispectral Analysis and Bilinear Time Series Models,* Vol. 24 of *Lecture Notes in Statistics* (Springer-Verlag, Berlin, 1984).
[47]R. J. Deissler, J. Stat. Phys. **40**, 371 (1985); Physica D **25**, 233 (1987).

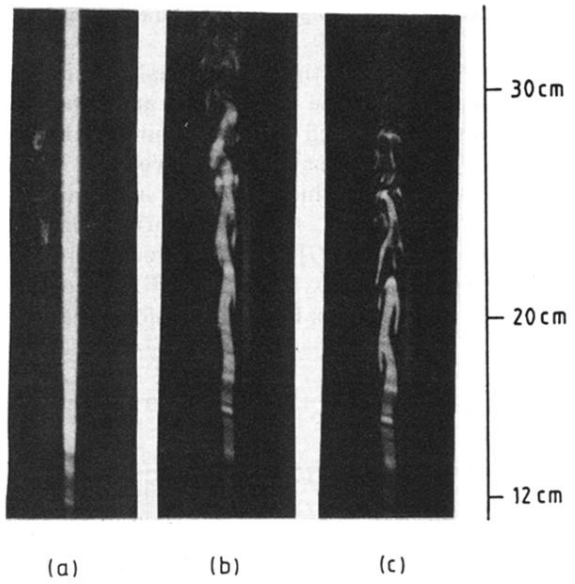

FIG. 2. Laser-light sheet flow visualization of the seeded jet. (a) The nonexcited jet at $R=500$. Top of scale is located at $X/D=61$. (b) and (c) Stroboscopic flow visualization of the excited seeded jet: $f_0=20$ Hz, $R=500$, normalized rms velocity fluctuation $u/U=0.4\%$ (b) and 0.6% (c). Notice the weakly turbulent region where the helical structure is no longer visible.